

1

Abstract

2

Measurement of total hadronic differential cross sections in the LArIAT experiment

3

4

Elena Gramellini

5

2018

6

Abstract goes here. Limit 750 words.

7 **Measurement of total hadronic differential**
8 **cross sections in the LArIAT experiment**

9 A Dissertation
10 Presented to the Faculty of the Graduate School
11 of
12 Yale University
13 in Candidacy for the Degree of
14 Doctor of Philosophy

15 by
16 Elena Gramellini

17 Dissertation Director: Bonnie T. Fleming

18 Date you'll receive your degree

21

A mia mamma e mio babbo,

22

grazie per le radici e grazie per le ali.

23

To my mom and dad,

24

thank you for the roots and thank you for the wings.

Contents

26	Acknowledgements	vi
27	0 Total Hadronic Cross Section Measurement Methodology	1
28	0.1 Event Selection	2
29	0.1.1 Selection of Beamline Events	2
30	0.1.2 Particle Identification in the Beamline	3
31	0.1.3 TPC Selection: Halo Mitigation	3
32	0.1.4 TPC Selection: Shower Removal	4
33	0.2 Beamline and TPC Handshake: the Wire Chamber to TPC Match . .	5
34	0.3 The Thin Slice Method	7
35	0.3.1 Cross Sections on Thin Target	7
36	0.3.2 Not-so-Thin Target: Slicing the Argon	8
37	0.3.3 Corrections to the Raw Cross Section	10
38	0.4 Procedure testing with truth quantities	11
39	1 Data and MC preparation for the Cross Section Measurements	14
40	1.1 Cross Section Analyses Data Sets	14
41	1.2 Construction of a Monte Carlo Simulation for LArIAT	16
42	1.2.1 G4Beamline	16
43	1.2.2 Data Driven MC	20
44	1.3 Estimate of Backgrounds in the Pion Cross Section	22

45	1.3.1	Background from Pion Capture and Decay	24
46	1.3.2	Contributions from the Beamline Background	27
47	1.4	Estimate of Energy Loss before the TPC	30
48	1.5	Tracking Studies	34
49	1.5.1	Study of WC to TPC Match	34
50	1.5.2	Tracking Optimization	37
51	1.5.3	Angular Resolution	37
52	1.6	Calorimetry Studies	42
53	1.6.1	Energy Calibration	42
54	1.6.2	Kinetic Energy Measurement	44
55	2	Negative Pion Cross Section Measurement	48
56	2.1	Raw Cross Section	48
57	2.1.1	Statistical Uncertainty	50
58	2.1.2	Treatment of Systematics	52
59	2.2	Corrections to the Raw Cross Section	53
60	2.2.1	Background subtraction	53
61	2.2.2	Efficiency Correction	56
62	2.3	Results	58
63	A	Kaon Analysis	60
64	A.1	Data Sample	60
65	A.2	Beamline Contamination	60
66	A.3	WC2TPC match	60
67	A.4	Cross Section	60
68	A.5	Future developments	60

69 Acknowledgements

70 *“Dunque io ringrazio tutti quanti.*

71 *Specie la mia mamma che mi ha fatto così funky.”*

72 – Articolo 31, Tanqi Funky, 1996 –

73 *“At last, I thank everyone.*

74 *Especially my mom who made me so funky.”*

75 – Articolo 31, Tanqi Funky, 1996 –

76 A lot of people are awesome, especially you, since you probably agreed to read
77 this when it was a draft.

Chapter 0

Total Hadronic Cross Section Measurement Methodology

This chapter describes the general procedure employed to measure a total hadronic differential cross section in LArIAT. Albeit with small differences, both the (π^-, Ar) and (K^+, Ar) total hadronic cross section measurements rely on the same procedure described in details in the following sections. We start by selecting the particle of interest using a combination of beamline detectors and TPC information (Section 0.1). We then perform a handshake between the beamline information and the TPC tracking to assure the selection of the right TPC track (Section 0.2). Finally, we apply the “thin slice” method and measure the “raw” hadronic cross section (Section 0.3). A series of corrections are then evaluated to obtain the “true” cross section (Section 0.3.3).

At the end of this chapter, we show a sanity check of the methodology by applying the thin slice method employing only MC truth information and retrieving the Geant4 tabulated cross section for pions and kaons (Section 0.4).

0.1 Event Selection

The measurement of the (π^- ,Ar) and (K^+ ,Ar) total hadronic cross section in LArIAT starts by selecting the pool of pion or kaon candidates and measuring their momentum. This is done through the series of selections on beamline and TPC information described in the next sections. The summary of the event selection in data is reported in Table 1.

0.1.1 Selection of Beamline Events

As shown in equation 5, we leverage the beamline particle identification and momentum measurement before entering the TPC as input to evaluate the kinetic energy for the hadrons used in the cross sections measurements. Thus, we select the LArIAT data to keep only events whose wire chamber and time of flight information is registered (line 1 in in Table 1). Additionally, we perform a check of the plausibility of the trajectory inside the beamline detectors: given the position of the hits in the four wire chambers, we make sure the particle's trajectory does not cross any impenetrable material such as the collimator and the magnets steel (line 2 in in Table 1).

	Run-II Neg Pol	Run-II Pos Pol
1. Events Reconstructed in Beamline	158396	260810
2. Events with Plausible Trajectory	147468	240954
3. Beamline $\pi^-/\mu^-/e^-$ Candidate	138481	N.A.
4. Beamline K^+ Candidate	N.A	2837
5. Events Surviving Pile Up Filter	108929	2389
6. Events with WC2TPC Match	41757	1081
7. Events Surviving Shower Filter	40841	N.A.
8. Available Events For Cross Section	40841	1081

Table 1: Number of data events for Run-II Negative and Positive polarity

109 **0.1.2 Particle Identification in the Beamline**

110 In data, the main tool to establish the identity of the hadron of interest is the LArIAT
 111 tertiary beamline, in its function of mass spectrometer. We combine the measurement
 112 of the time of flight, TOF , and the beamline momentum, p_{Beam} , to reconstruct the
 113 invariant mass of the particles in the beamline, m_{Beam} , as follows

$$m_{Beam} = \frac{p_{Beam}}{c} \sqrt{\left(\frac{TOF * c}{l}\right)^2 - 1}, \quad (1)$$

114 where c is the speed of light and l is the length of the particle's trajectory between
 115 the time of flight paddels.

116 Figure 1 shows the mass distribution for the Run II negative polarity runs on the
 117 left and positive polarity runs on the right. We perform the classification of events
 118 into the different samples as follows:

- 119 • $\pi/\mu/e$: mass < 350 MeV
- 120 • kaon: 350 MeV < mass < 650 MeV
- 121 • proton: 650 MeV < mass < 3000 MeV.

122 Lines 3 and 4 in in Table 1 show the number of negative $\pi/\mu/e$ and positive K
 123 candidates which pass the mass selection for LArIAT Run-II data.

124 **0.1.3 TPC Selection: Halo Mitigation**

125 The secondary beam impinging on LArIAT secondary target produces a plethora of
 126 particles which propagates downstream. The presence of upstream and downstream
 127 collimators greatly abates the number of particles tracing down the LArIAT tertiary
 128 beamline. However, it is possible that more than one particle sneaks into the LArTPC
 129 during its readout time: the TPC readout is triggered by the particle firing the

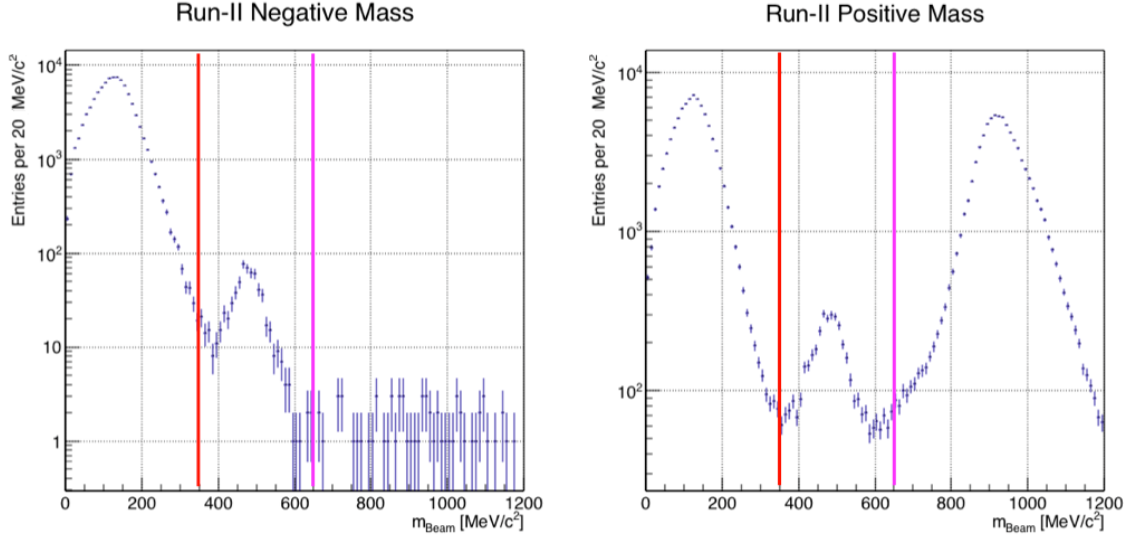


Figure 1: Distribution of the beamline mass as calculated according to equation 1 for the Run-II events reconstructed in the beamline, negative polarity runs on the left and positive polarity runs on the right. The classification of the events into $\pi^\pm/\mu^\pm/e^\pm$, K^\pm , or (anti)proton is based on these distributions, whose selection cut are represented by the vertical colored lines.

beamline detectors, but particles from the beam halo might be present in the TPC at the same time. We call “pile up” the additional traces in the TPC. We adjusted the primary beam intensity between LArIAT Run I and Run II to reduce the presence of events with high pile up particles in the data sample. For the cross section analyses, we remove events with more than 4 tracks in the first 14 cm upstream portion of the TPC from the sample (line 5 in in Table 1).

0.1.4 TPC Selection: Shower Removal

In the case of the (π^-, Ar) cross section, the resolution of beamline mass spectrometer is not sufficient to select a beam of pure pions. In fact, muons and electrons survive the selection on the beamline mass. It is important to notice that the composition of the negative polarity beam is mostly pions, as will be discussed in section 1.2.1. Still, we devise a selection on the TPC information to mitigate the presence of electrons

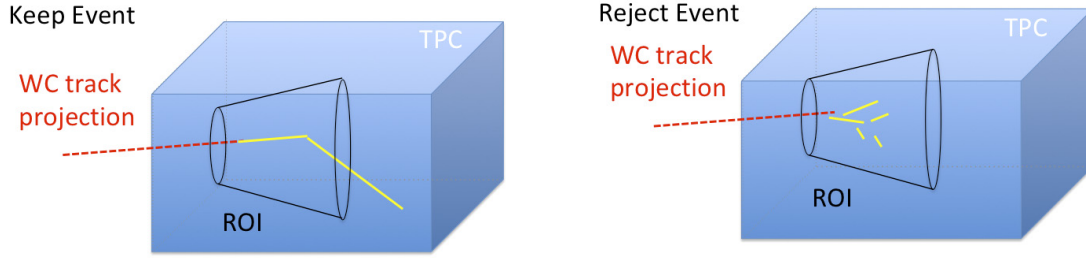


Figure 2: Visual rendering of the shower filter. The ROI is a cut cone, with a small radius of 4 cm, a big radius of 10 cm and an height of 42 cm (corresponding to 3 radiation lengths for electrons in Argon).

142 in the sample used for the pion cross section. The selection relies on the different
 143 topologies of a pion and an electron event in the argon: while the former will trace
 144 a track inside the TPC active volume, the latter will tend to “shower”, i.e. interact
 145 with the medium, producing bremsstrahlung photons which pair convert into several
 146 short tracks. In order to remove the shower topology, we create a region of interest
 147 (ROI) around the TPC track corresponding to the beamline particle. We look for
 148 short tracks contained in the ROI, as depicted in figure 4: if more then 5 tracks
 149 shorter than 10 cm are in the ROI, we reject the event. Line 7 in in Table 1 shows
 150 the number of events surviving this selection.

151 **0.2 Beamline and TPC Handshake: the Wire Cham-** 152 **ber to TPC Match**

153 For each event passing the selection on its beamline information, we need to identify
 154 the track inside the TPC corresponding to the particle which triggered the beamline
 155 detectors, a procedure we refer to as “WC to TPC match” (WC2TPC for short).
 156 In general, the TPC tracking algorithm will reconstruct more than one track in the
 157 event, partially due to the fact that hadrons interact in the chamber and partially
 158 because of pile up particles during the triggered TPC readout time, as shown in

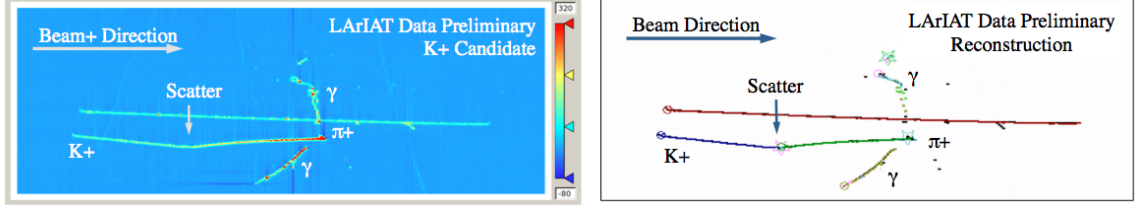


Figure 3: Kaon candidate event: on the right, event display showing raw quantities; on the left, event display showing reconstructed tracks. In the reconstructed event display, different colors represent different track objects. A kink is visible in the kaon ionization, signature of a hadronic interaction: the tracking correctly stops at the kink position and two tracks are formed. An additional pile-up track is so present in the event (top track in red).

figure 3.

We attempt to uniquely match one wire chamber track to one and only one reconstructed TPC track. In order to determine if a match is present, we apply a geometrical selection on the relative the position of the wire chamber and TPC tracks. We start by considering only TPC tracks whose first point is in the first 2 cm upstream portion of the TPC for the match. We project the wire chamber track to the TPC front face where we define the coordinates of the projected point as x_{FF} and y_{FF} . For each considered TPC track, we define ΔX as the difference between the x position of the most upstream point of the TPC track and x_{FF} . ΔY is defined analogously. We define the radius difference, ΔR , as $\Delta R = \sqrt{\Delta X^2 + \Delta Y^2}$. We define as α the angle between the incident WC track and the TPC track in the plane that contains them. If $\Delta R < 4$ cm, $\alpha < 8^\circ$, a match between WC-track and TPC track is found. We describe how we determine the value for the radius and angular selection in Section 1.5.1. We discard events with multiple WC2TPC matches. We use only those TPC tracks that are matched to WC tracks in the cross section calculation. Line 6 in Table 1 shows the number of events where a unique WC2TPC match was found.

In MC, we mimic the matching between the WC and the TPC track by constructing a fake WC track using truth information at wire chamber four. We then apply the same WC to TPC matching algorithm as in data.

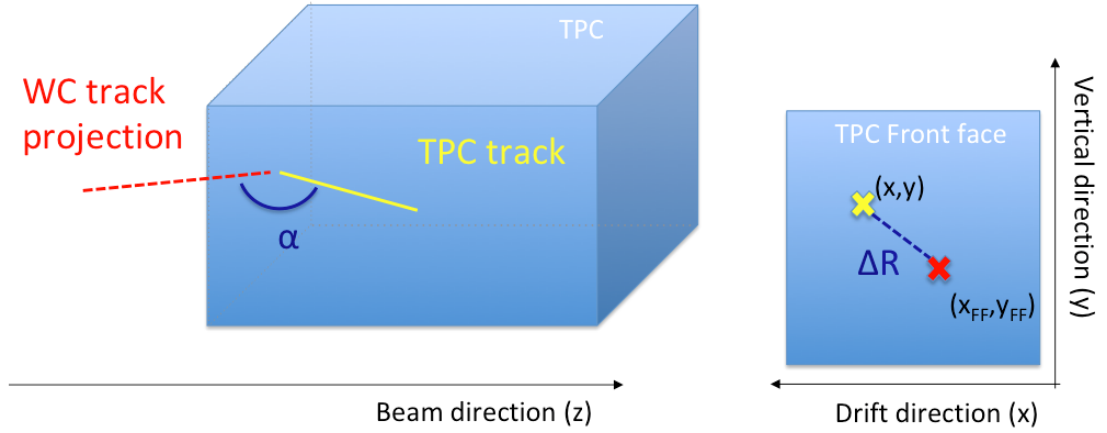


Figure 4: Visual rendering of the wire chamber to TPC match.

0.3 The Thin Slice Method

Once we have selected the pool of hadron candidates and we have identified the TPC track corresponding to the beamline event, we apply the thin slice method to measure the cross section, as the following sections describe.

0.3.1 Cross Sections on Thin Target

Cross section measurements on a thin target have been the bread and butter of nuclear and particle experimentalists since the Geiger-Marsden experiments [66]. At their core, this type of experiments consists in shooting a beam of particles with a known flux on a thin slab of material and recording the outgoing flux.

In general, the target is not a single particle, but rather a slab of material containing many diffusion centers. The so-called “thin target” approximation assumes that the target centers are uniformly distributed in the material and that the target is thin compared to the projectile interaction length, so that no center of interaction sits in front of another. In this approximation, the ratio between the number of particles interacting in the target N_{Int} and number of incident particles N_{Inc} on the target determines the interaction probability $P_{\text{Interacting}}$, which is the complementary to one

194 of the survival probability $P_{Survival}$. Equation 2

$$P_{Survival} = 1 - P_{Interacting} = 1 - \frac{N_{Int}}{N_{Inc}} = e^{-\sigma_{TOT}n\delta X} \quad (2)$$

195 describes the probability for a particle to survive the thin target. This formula relates
 196 the interaction probability to the total hadronic cross section (σ_{TOT}), the density of
 197 the target centers (n)¹ and the thickness of the target along the incident hadron
 198 direction (δX). If the target is thin compared to the interaction length of the process
 199 considered, we can Taylor expand the exponential function in equation 2 and find
 200 a simple proportionality relationship between the cross section and the number of
 201 incident and interacting particles, as shown in equation 3:

$$1 - \frac{N_{Int}}{N_{Inc}} = 1 - \sigma_{TOT}n\delta X + O(\delta X^2). \quad (3)$$

202 Solving for the cross section, we find:

$$\sigma_{TOT} = \frac{1}{n\delta X} \frac{N_{Int}}{N_{Inc}}. \quad (4)$$

203 **0.3.2 Not-so-Thin Target: Slicing the Argon**

204 The interaction length of pions and kaons in argon is expected to be of the order
 205 of 50 cm for pions and 100 cm for kaons. Thus, the LArIAT TPC, with its 90 cm
 206 of length, is not a thin target. However, the fine-grained tracking of the LArIAT
 207 LArTPC allows us to treat the argon volume as a sequence of many adjacent thin
 208 targets.

209 As described in Chapter ??, LArIAT wire planes consist of 240 wires each. The
 210 wires are oriented at +/- 60° from the vertical direction at 4 mm spacing, while the

1. The scattering center density in the target, n , relates to the argon density ρ , the Avogadro number N_A and the argon molar mass m_A as $n = \frac{\rho N_A}{m_A}$.

beam direction is oriented 3 degrees off the z axis in the XZ plane. The wires collect signals proportional to the energy loss of the hadron along its path in a $\delta X = 4$ mm/ $(\sin(60^\circ)\cos(3^\circ)) \approx 4.7$ mm slab of liquid argon. Thus, one can think to slice the TPC into many thin targets of $\delta X = 4.7$ mm thickness along the direction of the incident particle, making a measurement at each wire along the path.

Considering each slice j a “thin target”, we can apply the cross section calculation from Equation 2.1 iteratively, evaluating the kinetic energy of the hadron as it enters each slice, E_j^{kin} . For each WC2TPC matched particle, the energy of the hadron entering the TPC is known thanks to the momentum and mass determination by the tertiary beamline,

$$E_{FrontFace}^{kin} = \sqrt{p_{Beam}^2 - m_{Beam}^2} - m_{Beam} - E_{loss}, \quad (5)$$

where E_{loss} is a correction for the energy loss in the uninstrumented material between the beamline and the TPC front face. The energy of the hadron at each slab is determined by subtracting the energy released by the particle in the previous slabs. For example, at the j^{th} point of a track, the kinetic energy will be

$$E_j^{kin} = E_{FrontFace}^{kin} - \sum_{i < j} E_{Dep,i}, \quad (6)$$

where $E_{Dep,i}$ is the energy deposited at each argon slice before the j^{th} point as measured by the calorimetry associated with the tracking.

If the particle enters a slice, it contributes to $N_{Inc}(E^{kin})$ in the energy bin corresponding to its kinetic energy in that slice. If it interacts in the slice, it also contributes to $N_{Int}(E^{kin})$ in the appropriate energy bin. The cross section as a function of kinetic energy, $\sigma_{TOT}(E^{kin})$ will then be proportional to the ratio $\frac{N_{Int}(E^{kin})}{N_{Inc}(E^{kin})}$.

Our goal is to measure the total interaction cross section, independently from the topology of the interaction. Thus, we determine that a hadron interacted simply by

	min	max
X	1 cm	46 cm
Y	-15 cm	15 cm
Z	0 cm	86 cm

Table 2: Fiducial volume boundaries used to determine cross section interaction point.

233 requiring that the last point of the WC2TPC matched track lies inside the fiducial
234 volume, whose boundaries are defined in Table 2. If the TPC track stops within the
235 fiducial volume, its last point will be the interaction point; if the track crosses the
236 boundaries of the fiducial volume, the track will be considered “through going” and
237 no interaction point will be found. The only slabs considered to fill the N_{Inc} and
238 N_{Inc} plots are the slabs included the fiducial volume.

239 0.3.3 Corrections to the Raw Cross Section

240 Equation 2.1 is a prescription for measuring the cross section in case of a pure beam
241 of the hadron of interest and 100% efficiency in the determination of the interaction
242 point. For example, if LArIAT had a beam of pure pions and were 100% efficient
243 in determining the interaction point within the TPC, the pion cross section in each
244 energy bin would be given by

$$\sigma_{TOT}^{\pi^-}(E_i) = \frac{1}{n\delta X} \frac{N_{\text{Int}}^{\pi^-}(E_i)}{N_{\text{Inc}}^{\pi^-}(E_i)}. \quad (7)$$

245 Unfortunately, this is not the case. In fact, the selection used to isolate pions
246 in the LArIAT beam allows for the presence of some muons and electrons as back-
247 ground. Also, the LArIAT TPC is not 100% efficient in determining the interaction
248 point. Therefore we need to apply two corrections evaluated on the MC in order to
249 extract the true cross section from LArIAT data: the background subtraction and
250 the efficiency correction. Still using the pion case as example, we estimate the pion

251 cross section in each energy bin changing Equation 7 into

$$\sigma_{TOT}^{\pi^-}(E_i) = \frac{1}{n\delta X} \frac{N_{\text{Int}}^{\pi^-}(E_i)}{N_{\text{Inc}}^{\pi^-}(E_i)} = \frac{1}{n\delta X} \frac{\epsilon^{\text{Inc}}(E_i)[N_{\text{Int}}^{\text{TOT}}(E_i) - B_{\text{Int}}(E_i)]}{\epsilon^{\text{Int}}(E_i)[N_{\text{Inc}}^{\text{TOT}}(E_i) - B_{\text{Inc}}(E_i)]}, \quad (8)$$

252 where $N_{\text{Int}}^{\text{TOT}}(E_i)$ and $N_{\text{Incident}}^{\text{TOT}}(E_i)$ is the measured content of the interacting and
 253 incident histograms for events that pass the event selection, $B_{\text{Int}}(E_i)$ and $B_{\text{Inc}}(E_i)$
 254 represent the contributions from beamline background to the interacting and incident
 255 histograms respectively, and $\epsilon^{\text{Int}}(E_i)$ and $\epsilon^{\text{Inc}}(E_i)$ are the efficiency corrections for said
 256 histograms.

257 As we will show in section 1.3, the background subtraction for the interacting
 258 and incident histograms can be translated into a corresponding relative pion content
 259 $C_{\text{Interacting}}^{\pi MC}(E_i)$ and $C_{\text{Incident}}^{\pi MC}(E_i)$ and the cross section re-written as follows

$$\sigma_{TOT}^{\pi^-}(E_i) = \frac{1}{n\delta X} \frac{\epsilon^{\text{Inc}}(E_i)}{\epsilon^{\text{Int}}(E_i)} \frac{C_{\text{Int}}^{\pi MC}(E_i)}{C_{\text{Inc}}^{\pi MC}(E_i)} \frac{N_{\text{Int}}^{\text{TOT}}(E_i)}{N_{\text{Inc}}^{\text{TOT}}(E_i)}. \quad (9)$$

260 0.4 Procedure testing with truth quantities

261 The (π^-, Ar) and (K^+, Ar) total hadronic cross section implemented in Geant4 can be
 262 used as a tool to validate the measurement methodology. We describe here a closure
 263 test done on Monte Carlo to prove that the methodology of slicing the TPC retrieves
 264 the underlying cross section distribution implemented in Geant4 within the statistical
 265 uncertainty.

266 For pions and kaons in the considered energy range, the Geant4 inelastic model
 267 adopted is “BertiniCascade”; the pion elastic cross sections are modeled on Chips,
 268 while the kaon elastic cross sections are modeled on Gheisha and Chips.

269 For the validation test, we fire a sample of pions and a sample of kaons inside
 270 the LArIAT TPC active volume using the Data Driven Monte Carlo (see section
 271 1.2.2). We apply the thin-sliced method using only true quantities to calculate the

272 hadron kinetic energy at each slab in order to decouple reconstruction effects from
 273 possible issues with the methodology. For each slab of 4.7 mm length along the
 274 path of the hadron, we integrate the true energy deposition as given by the Geant4
 275 transportation model. Then, we recursively subtracted it from the hadron kinetic
 276 energy at the TPC front face to evaluate the kinetic energy at each slab until the
 277 true interaction point is reached. Since the MC is a pure beam of the hadron of
 278 interest and truth information is used to retrieve the interaction point, no correction
 279 is applied. Doing so, we obtain the true interacting and incident distributions for
 280 the considered hadron and we obtain the true MC cross section as a function of the
 281 hadron true kinetic energy.

282 Figure 5 shows the total hadronic cross section for argon implemented in Geant4
 283 10.03.p1 (solid lines) overlaid with the true MC cross section as obtained with the
 284 sliced TPC method (markers) for pions on the left and kaons on the right; the total
 285 cross section is shown in green, the elastic cross section in blue and the inelastic
 286 cross section in red. The nice agreement with the Geant4 distribution and the cross
 287 section obtained with the sliced TPC method gives us confidence in the validity of
 288 the methodology.

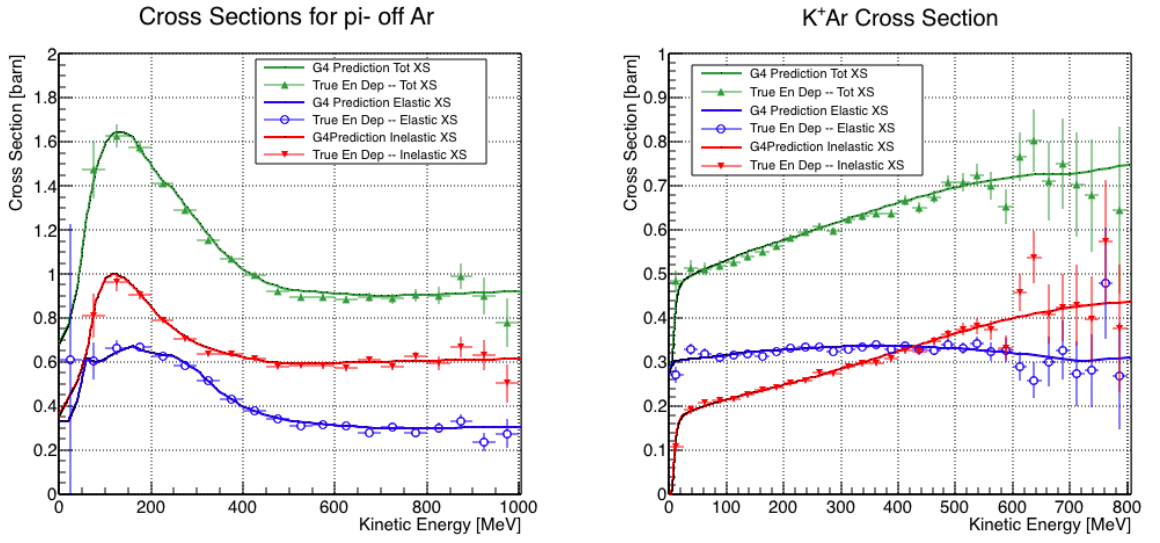


Figure 5: Hadronic cross sections for (π^-, Ar) on the left and (K^+, Ar) on the right as implemented in Geant4 10.03.p1 (solid lines) overlaid the true MC cross section as obtained with the sliced TPC method (markers). The total cross section is shown in green, the elastic cross section in blue and the inelastic cross section in red.

Chapter 1

Data and MC preparation for the Cross Section Measurements

This chapter describes the preparatory work done on the the data and Monte Carlo samples used for the cross section analyses. This entails the choice of the datasets and the production of the information needed to construct the Monte Carlo Simulation (section 1.1), the construction and use of said Monte Carlo simulation (section 1.2), the study and optimization of the tracking in the TPC for the cross section analyses (section 1.5), the calibration of the calorimetry response and related energy studies (section 1.6).

1.1 Cross Section Analyses Data Sets

We choose LArIAT Run-II as the data period for the (π^-, Ar) and (K^+, Ar) total hadronic cross section analyses. Data taking for the this period started on 03/15/2016 and ended on 07/31/2016. Since we are interested in beamline and TPC information, we ask basic requirements on the operational status of the time of fight, wire chambers and TPC to form the good run list for this period, which we informally call “lovely runs”.

306 The subset of lovely runs chosen for the (π^-, Ar) total hadronic cross section
 307 analysis includes only the -60A and -100A magnet configurations in negative polarity,
 308 even if LArIAT explored several other beamline configurations during Run-II. The
 309 -60A and -100A combined data set accounts for approximately 90% of the total Run-
 310 II negative polarity runs. The choice of the main two beamline settings limits the
 311 need for the production of many MC sets and related corrections, still maintaining a
 312 high number of events.

313 Similarly, the subset of lovely runs chosen for the (K^+, Ar) total hadronic cross
 314 section analysis includes only the +60A and +100A magnet configurations in positive
 315 polarity. It should be noted that kaons are extremely rare in the +60A sample, thus
 316 the data sample for the (K^+, Ar) cross section after the mass selection is about 90%
 317 +100A runs, as shown in Table 1.1.

318 For the first measurements in LArIAT that uses both beamline and TPC infor-
 319 mation, we choose strict requirements on the reconstruction of the WC tracks, the
 320 so-called “Picky Track” sample (see Section ??). This choice presents two advantages:
 321 the uncertainty on the momentum reconstruction for the “Picky Tracks” sample is
 322 smaller compared to the “High Yield” sample, and the comparison with the beam-
 323 line MC results is straightforward. A possible future update and cross check of these
 324 analysis would be the use of the High Yield sample, where the statistics is about three
 325 times higher.

326 The breakdown of beamline events as a function of the magnets settings is shown
 327 in Table 1.1. The choice of the data sets determines the production of beamline MC
 328 and serves as basis for the production of Data Driven MC, as shown in the next
 329 sections.

1.2 Construction of a Monte Carlo Simulation for LArIAT

For the simulation of LArIAT events and for the simulation of the datasets' particle make up, we use a combination of two MC generators: the G4Beamline Monte Carlo and the Data Driven single particle Monte Carlo (DDMC). We use the G4Beamline MC to simulate the particle transportation in the beamline and calculate the particle composition of the beam just after the fourth Wire Chamber (WC4). In order to simulate the beamline particles after WC4 and in the TPC, we use the DDMC.

1.2.1 G4Beamline

G4Beamline simulates the beam collision with the LArIAT secondary target, the energy deposited by the particles in the LArIAT beamline detectors, and the action of the LArIAT magnets, effectively accounting for particle transportation through the beamline from the LArIAT target until “Big Disk”, a fictional, void detector located just before the LArIAT cryostat. At the moment of this writing, G4Beamline does not simulated the responses of the beamline detectors. It is possible to interrogate the truth level information of the simulated particles in several points of the geometry. In order to ease the handshake between G4Beamline and the DDMC, we ask for the beam composition just after WC4. Since LArIAT data are taken under different beam conditions, we need to simulate separately the beam composition according to the magnets' settings and the secondary beam intensity with G4Beamline. For the

	I = 60 A	I = 100 A	Total
Data Events after $\pi/\mu/e$ Mass Selection	67068	71413	138481
Data Events after K Mass Selection	274	2563	2837

Table 1.1: Number of data events which fit the $\pi/\mu/e$ or K mass hypothesis as a function of magnet settings.

pion cross section analysis the relevant beam conditions are secondary beam energy of 64 GeV, negative polarity magnet with current of 100 A and 60 A. For the kaon cross section analysis the relevant beam conditions is a secondary beam energy of 64 GeV, positive polarity magnet with current of 100 A.

Beam Composition for Negative Pion Cross Section

Even if pions are by far the biggest beam component in negative polarity runs, the LArIAT tertiary beam is not a pure pion beam. While useful to discriminate between pions, kaons, and protons, the beamline detectors are not sensitive enough to discriminate among the lighter particles in the beam: electrons, muons and pions fall under the same mass hypothesis. Thus, we need to assess the contamination from beamline particles other than pions in the event selections used for the pion cross section analysis and correct for its effects. The first step of this process is assessing the percentage of electrons and muons in the $\pi/\mu/e$ beamline candidates via the G4Beamline MC. Since the beamline composition is a function of the magnet settings, we simulate separately events for magnet current of -60A and -100A. Figure 1.1 shows the momentum predictions from G4Beamline overlaid with data for the 60A runs (left) and for the 100A runs (right). The predictions for electrons, muons and pions have been staggered and their sum is area normalized to data. Albeit not perfect, these plots show a reasonable agreement between the momentum shapes in data and MC. We attribute the difference in shape to the lack of simulation of the WC efficiency in the MC which is momentum dependent and leads to enhance the number events in the center of the momentum distribution.

Table 1.2 shows the beam composition per magnet setting after the mass selection according to the G4Beamline simulation.

The estimated beam composition is used as a basis to estimate the background contamination in the (π^-, Ar) cross section measurement, whose full treatment is

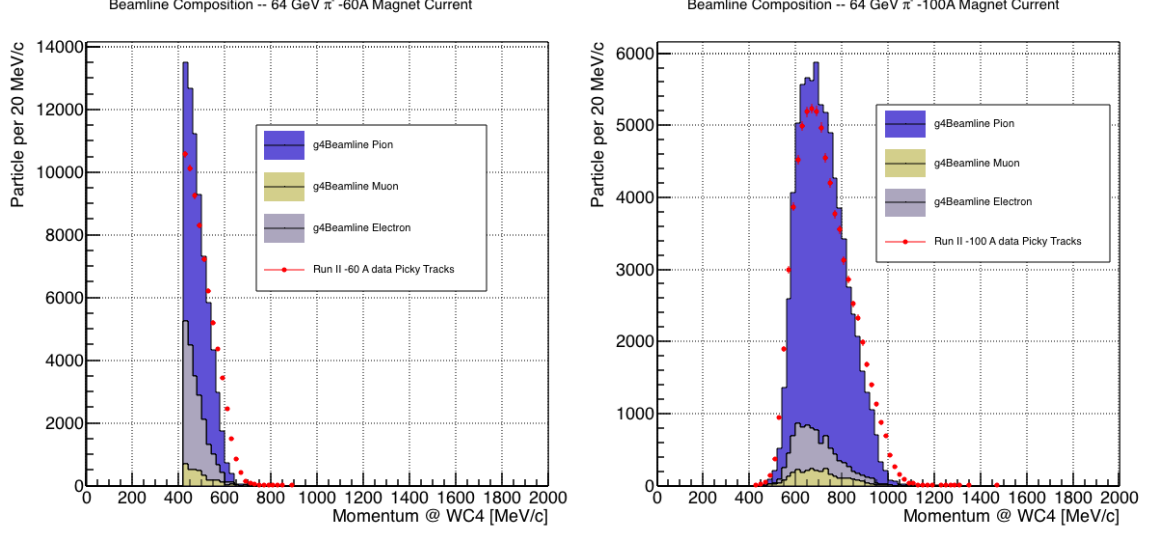


Figure 1.1: Beam composition for the -60A runs (left) and -100A runs (right). The solid blue plot represents the simulated pion content, the yellow plot represents the simulated muon content and the grey plot represents the simulated electron content. The plots are area normalized to the number of data events, shown in red.

	I = -60 A	I = -100 A
G4Pions	68.8 %	87.4 %
G4Muons	4.6 %	3.7 %
G4Electrons	26.6 %	8.9 %

Table 1.2: Simulated beamline composition per magnet settings

described in section 1.3.

Beam Composition for Positive Kaon Cross Section

In the positive polarity runs, the tertiary beam composition is mainly pions and protons. The left side of Figure 1.2 shows the predictions for the momentum spectra for the 100A positive runs according to G4Beamline (solid colors) overlaid with data (black points). Since the LArIAT beamline detectors can discriminate between kaons and other particles, we do not rely on the G4Beamline simulation to estimate the beamline contamination in the pool of kaon candidates (as in the case of the pion cross section), but rather we use a data drive approach. The basic idea of this data driven approach is to estimate the bleed over from high and low mass peaks under the kaon peak by fitting the tails of the $\pi/\mu/e$ and proton mass distributions, as shown in Figure 1.2 right side. Since the shape of the tails is unknown, the estimate is done multiple times varying the range and shape for reasonable functions. For example, to estimate the proton content under the kaon peak, we start by fitting the left tail of the proton mass distribution with a gaussian function between $650 \text{ MeV}/c^2$ and $750 \text{ MeV}/c^2$. We extend the fit function under the kaon peak and integrate the extended fit function between $350\text{-}650 \text{ MeV}/c^2$. We integrate the mass histogram in the same range and calculate the proton contamination as the ratio between the two integrals. We repeat this procedure for several fit shapes (gaussian, linear and exponential functions) and tail ranges. Finally, we calculate the contamination as the weighted average of single estimates, where the weights are calculated to be the $1./\chi^2$ of the tail fits. The procedure is repeated for lighter particles mass peak independently. With 12 iterations of this method we find a proton contamination of $0.2 \pm 0.5 \%$ and a contamination from the lighter particles of $5 \pm 2 \%$. The estimate of the proton background is currently not used in the kaon cross section analysis, but it is a fundamental step to retrieve the true kaon cross section which will be implemented

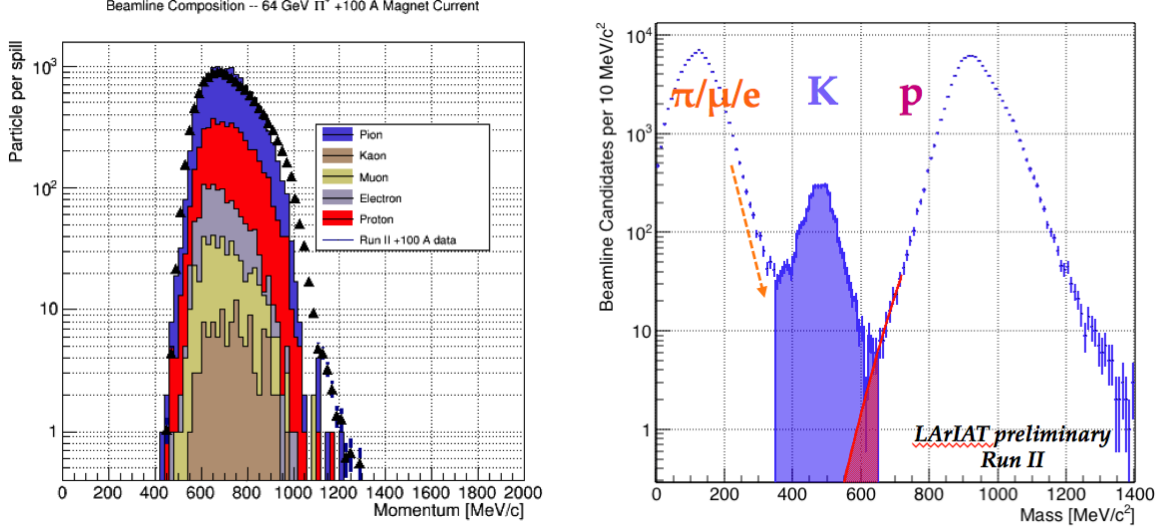


Figure 1.2: *Left*: Beam composition for the +100A runs after WC4 (no mass selection applied). The solid colors represent the contributions from the G4Beamline simulated particles: blue plot represents the simulated pion content, the yellow plot represents the simulated muon content and the grey plot represents the simulated positron content, the red the proton content and the mustard the kaon content. The plots are area normalized to the number of data events, shown in black. *Right*: Mass distribution for the Run-II positive runs, where the area under the kaon mass peak is highlighted in purple. The area under the extension of a possible fit for the proton tail is highlighted in red.

in the analysis next step.

1.2.2 Data Driven MC

The Data Driven single particle Monte Carlo (DDMC) is a single particle gun which simulates the particle transportation from WC4 into the TPC leveraging on the beamline data information. The DDMC uses the data momentum and position at WC4 to derive the event generation: a general sketch of the DDMC workflow is shown in Figure 1.3.

When producing a DDMC sample, beamline data from a particular running period and/or running condition are selected first. For example, data for the negative 60A runs and for the negative 100A runs inform the event generation stage of two different DDMC samples. Figure 1.4 schematically shows the data quantities of in-

413 terest leveraged from data: the momentum (P_x, P_y, P_z) and position (X, Y) at WC4.
 414 For each data event, we obtain the particle position (X, Y) at WC4 directly from the
 415 data measurement; we calculate the components of the momentum using the beamline
 416 measurement of the momentum magnitude in conjunction with the hits on WC3 and
 417 WC4 to determine the direction of the momentum vector, as described in section ??.
 418 The momentum and position of the selected data form a 5-dimensional tuple, which
 419 we sample thousands of times through a 5-dimensional hit-or-miss sampling proce-
 420 dure to generate the MC events. This generates MC events with the same momentum
 421 and position distributions as data, with the additional benefit of accounting for the
 422 correlations between the P_x, P_y, P_z, X, Y variables. As an example, the results of the
 423 DDMC generation compared to data for the kaon +100A sample are shown in figure
 424 1.5 for the P_z, X and Y distributions; as expected, MC and data agree within the
 425 statistical uncertainty by construction. A LArSoft simulation module then launches
 426 single particle MC from $z = -100$ cm (the location of the WC4) using the MC gener-
 427 ated events. The particles are free to decay and interact in their path from WC4 to
 428 the TPC according to the Geant4 simulation.

429 Using the DDMC technique ensures that the MC and data particles have very
 430 similar momentum, position and angular distributions at WC4 and allows us to use
 431 the MC sample in several occasions: to calibrate the energy loss upstream of the TPC
 432 (see Section 1.4), to estimate the background contamination to the pion cross section
 433 (see Section 1.3), or to study the tracking and the calorimetric performance (sections
 434 1.5 and 1.6). A small caveat is in order here: the DDMC is a single particle Monte
 435 Carlo, which means that the beam pile-up is not simulated.

436 Six samples are the basis for the MC used in the pion cross section measurement:
 437 three samples of ~ 340000 pions, muons and electrons to simulate the negative 60A
 438 runs, and three samples of ~ 340000 pions, muons and electrons for the negative 100A
 439 runs.

440

The MC used for the kaon cross section analysis is a sample of **NUMBERS** kaons.

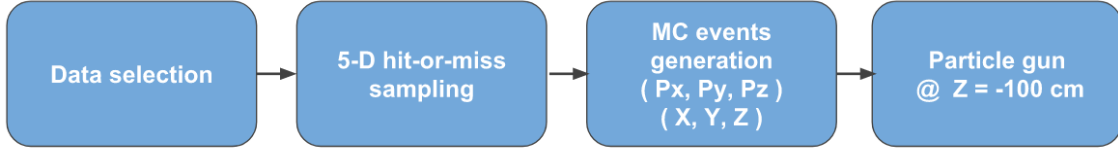


Figure 1.3: Workflow for Data Driven single particle Monte Carlo production.

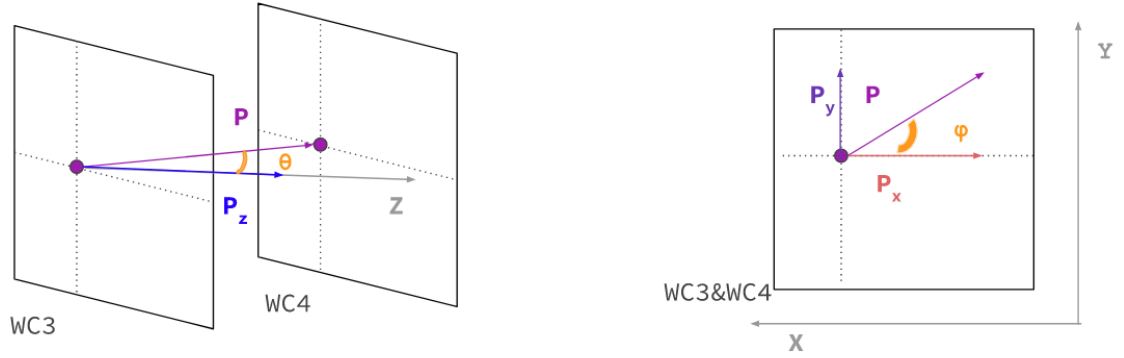


Figure 1.4: Scheme of the quantities of interest for the DDMC event generation: P_x, P_y, P_z, X, Y at WC4.

441

1.3 Estimate of Backgrounds in the Pion Cross

442

Section

443

We use the beamline simulation and the DDMC simulation to estimate the back-

444

ground in the total hadronic pion cross section. Two categories of background exists

445

for the negative pion cross section measurement: the one related to the pion interac-

446

tion in the chamber, discussed in Section 1.3.1 and the one related to the beamline

447

contamination, discussed in Section 1.3.2.

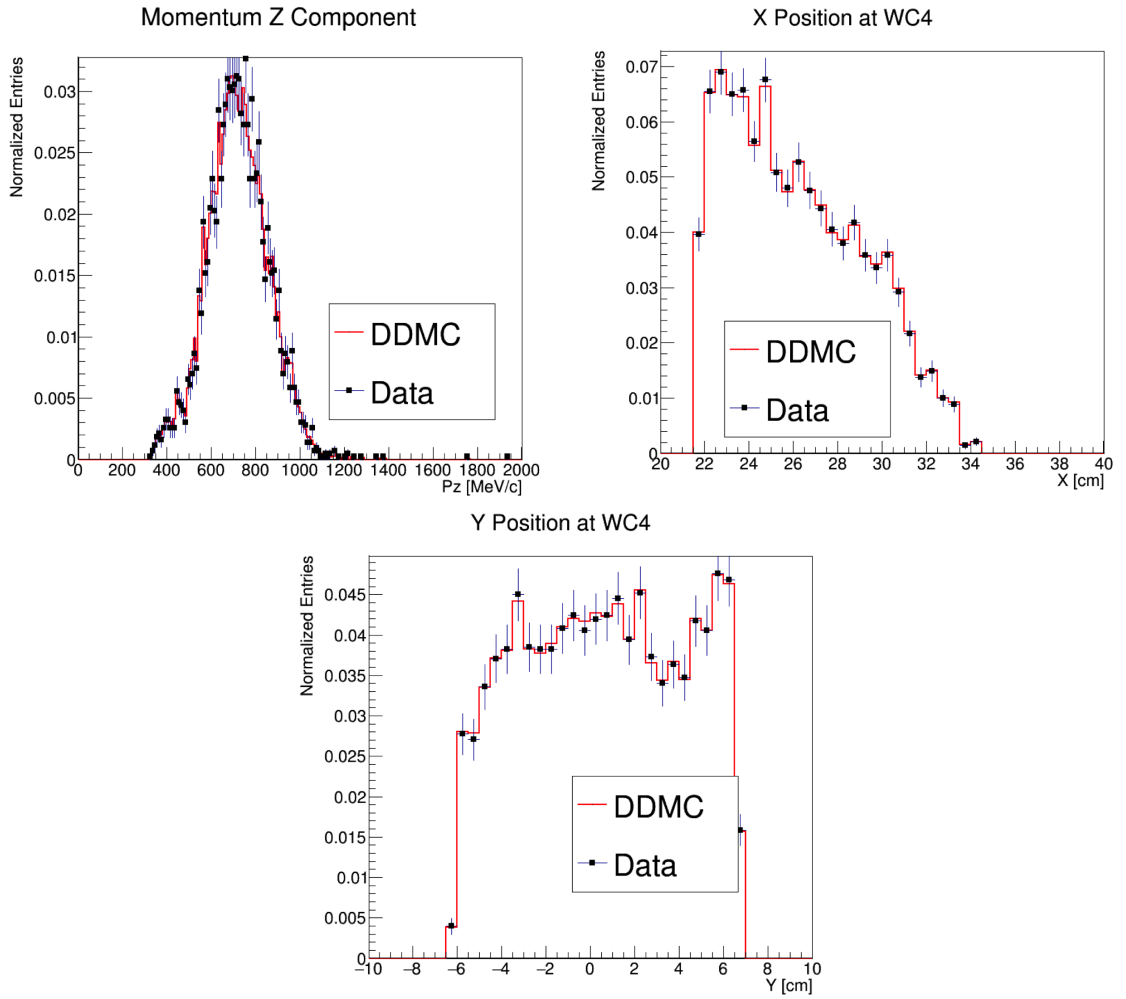


Figure 1.5: Comparison between generated quantities and data distributions for the 100A kaon sample: Z component of the momentum at WC4 (top left), X position at Wire Chamber 4 (top right), Y position at Wire Chamber 4 (bottom).

1.3.1 Background from Pion Capture and Decay

Our goal is to measure the total hadronic cross section for negative pions in argon. Since pion capture can be classified as an electromagnetic process and pion decay is a weak process, capture and decay represent unwanted interactions. We present here a study of capture and decay in Monte Carlo and the solution we adopted to mitigate their occurrence in the data sample.

For this MC study, we use a sample of MC pions generated according to the -60A beam profile with the DDMC (see Section 1.2.2). It is important to notice that capture occurs predominantly at rest, while decay may occur both in flight and at rest. Thus, we can highly mitigate capture and decay at rest by removing pions which would release all their energy in the TPC and stop. This translates into a momentum selection, where we keep only events whose WC momentum is above a certain threshold. Figure 1.6 shows the true momentum distribution for the primary pions¹ that arrive to the TPC (pink), that capture (green) or decay (blue) inside the TPC, on a linear and log scale vertical axis.

In order to choose the selection value for the wire chamber momentum, it is beneficial to estimate the ratio of events which capture or decay that survive the selection in MC as a function of the momentum threshold, and compare it with the survival ratio for all events. This is done in figure 1.7. We define the survival ratio simply as the number of events surviving the true momentum selection divided by the number of events of that category. We calculate the survival ratio separately for the three event categories explained above: total (pink), capture (green) and decay (blue). Selecting pions with momentum greater than $420\text{ MeV}/c$ reduces the capture events by 99% while maintaining about 80% of the total data sample. Figure 1.8

1. We use here the Geant4 denomination “primary” to indicate that the pion considered does not undergo interactions modifying its energy before getting to the TPC. In fact, not every pion shot from wire chamber four will arrive to the TPC as primary, some will decay or interact before the TPC.

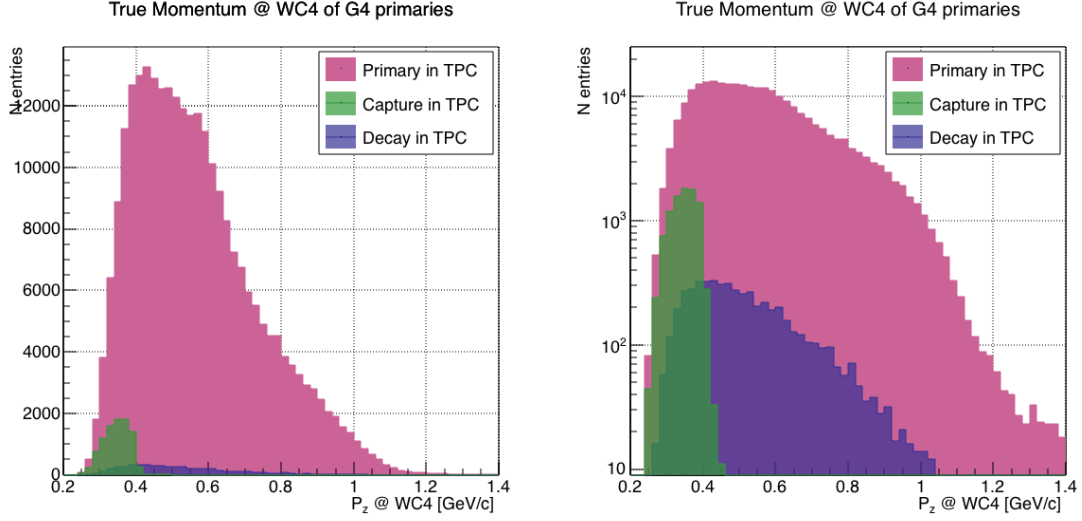


Figure 1.6: True momentum distribution at wire chamber 4 for every simulated pion arriving in the TPC (pink), ending its life in capture (green) or in decay (blue) in the TPC, linear vertical axis on the left, logarithmic on the right.

472 shows the ratio of events which end their life in capture (green) or decay (blue) over
 473 the total number of events as a function of the true momentum at wire chamber
 474 four. This ratio is slightly dependent on the inelastic cross section implemented in
 475 Geant4, as we are able to register a pion capture (or decay) only if it did not interact
 476 inelastically in the TPC. We choose a momentum threshold of 420 MeV/c because the
 477 percentage of capture events drops below 1% and the percentage of decays is never
 478 above 2% for momenta greater than 420 MeV/c. After the momentum selection, we
 479 evaluate the contribution of capture and decay to be a negligibly small background to
 480 the cross section measurement compared to the background related to the beamline.

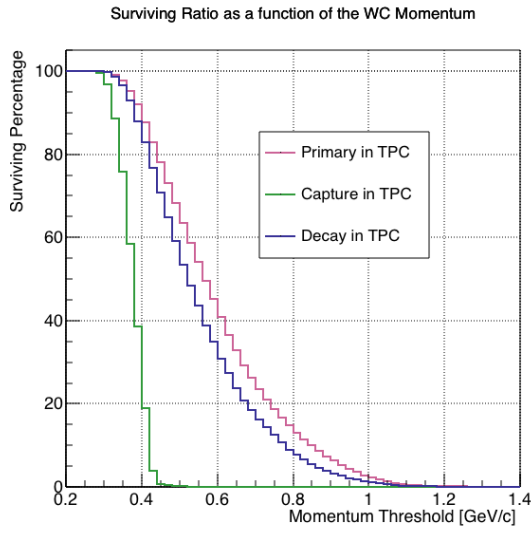


Figure 1.7: Survival ratio as a function of selection threshold on true momentum at wire chamber four for every simulated pion arriving in the TPC (pink), capture (green) or in decay (blue).

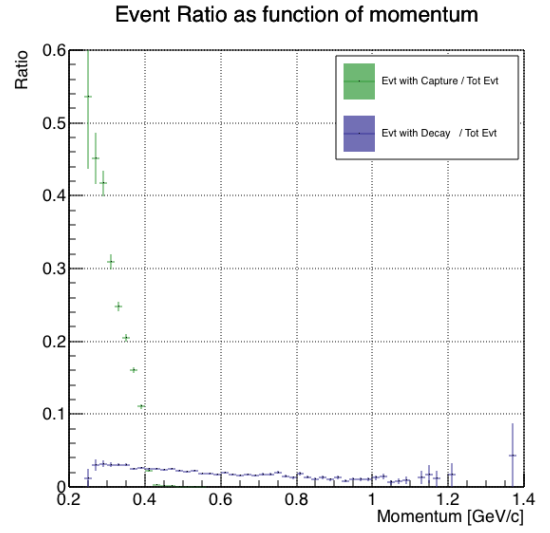


Figure 1.8: Ratio between the capture (green) and decay (blue) events over the total number of events as a function of the true momentum at wire chamber four.

1.3.2 Contributions from the Beamline Background

We define beamline background every TPC track matched to the WC track which is not a primary pion. Potentially, there are 4 different types of beamline background:

1) electrons,

2) muons,

3) secondaries from pion events,

4) matched pile up events.

The first step to quantify the effect of the beamline background on the pion cross section is to estimate what percentage of events used in the cross section calculation is not a primary pion. We start by noting that the last type of background, the “matched pile up” events, is a negligible fraction, because of the definition of the WC2TPC match: we deem the probability of a single match with a halo particle in the absence of a beamline particle² negligibly small. As shown in Section 1.2.1, we use G4Beamline to estimate the percentage of pions, muons and electrons at WC4, obtaining the composition shown in Table 1.2. The next step is to simulate those pions, muons and electrons from WC4 to the TPC with the DDMC and evaluate their contribution to the cross section. To do so, we start by simulating the same number of electrons, muons and pions with the DDMC and we apply the same selection filters on the three samples. The number of events per particle species surviving this selection is shown on table 1.3. In order to reproduce the closest make up of the beam to data, we weight each event of a given particle species according to the estimated beam composition. In case of 60A runs, for example, the weights are 0.688 for pions, 0.046 for muons and 0.266 for electrons.

2. Events with multiple WC2TPC matches are always rejected.

	Magnet Current -60A			Magnet Current -100 A		
	MC π^-	MC μ^-	MC e^-	MC π^-	MC μ^-	MC e^-
Total Initial events	334500	334500	334500	344500	344500	344500
After Multiplicity Rejection	330668	333420	198065	326576	344208	201380
After WC2TPC Selection	218239	296333	91139	230418	300228	98834
Evts After Shower Rejection	208063	288914	20293	219882	293585	17780
Selection Survival Rate	62.3%	86.6%	6.1%	63.8%	85.5%	5.2%
Beam Composition @WC4	68.8%	4.6 %	26.6 %	87.4 %	3.7 %	8.9 %
Beam Composition @TPC FF	88.5%	8.2%	3.3 %	94.0%	5.3%	0.7%

Table 1.3: MC selection flow per particle species.

504 It should be noted that pions may interact hadronically in the steel or in the
 505 non-instrumented argon upstream to the TPC front face while travelling the length
 506 of between WC4 and the TPC. Or, they could decay in flight between WC4 and the
 507 TPC. One of the interaction products can leak into the TPC and be matched with the
 508 WC track, contributing to the pool of events used for the cross section calculation. We
 509 call this type of particles “secondaries” from pion events, with a terminology inspired
 510 by Geant4. We estimate the number of secondaries using the DDMC pion sample.
 511 The percentage of secondaries is given by the number of matched WC2TPC tracks
 512 whose corresponding particle is not flagged as primary by Geant4. The secondary to
 513 pion ratio is 4.9% in the 60A sample and 4.3% in the 100A sample.

514 We evaluate the beamline background contribution to the cross section by pro-
 515 ducing the interacting and incident histograms for the events surviving the selection,
 516 staggering the contributions for each particle species, as shown in Figure 1.9. From
 517 those histograms, we are able to evaluate the contribution of pions and beamline
 518 backgrounds to each bin of the interacting and incident histograms separately and
 519 obtain the relative pion content. The relative pion content in each bin for the inter-
 520 acting and incident histograms represents the correction applied to data. We take

here the interacting histogram as example, noting that the derivation of the correction for the incident histogram is identical. The number of entries in each bin of the interacting plot (Figure 1.9 left) is $N_{\text{Int}}^{\text{TOT}}(E_i)$, equal to the sum of the pions and beamline backgrounds in that bin, namely

$$N_{\text{Int}}^{\text{TOT}}(E_i) = N_{\text{Int}}^{\pi}(E_i) + \underbrace{N_{\text{Int}}^{\mu}(E_i) + N_{\text{Int}}^e(E_i) + N_{\text{Int}}^{\text{Secondary}}(E_i)}_{B_{\text{Int}}(E_i)}. \quad (1.1)$$

Thus, the relative pion content to each bin in MC can be calculated as follows

$$C_{\text{Int}}^{\pi MC}(E_i) = \frac{N_{\text{Int}}^{\pi MC}}{N_{\text{Int}}^{\text{TOTMC}}(E_i)} = \frac{N_{\text{Int}}^{\text{TOTMC}}(E_i) - B_{\text{Int}}^{\text{MC}}(E_i)}{N_{\text{Int}}^{\text{TOTMC}}(E_i)}. \quad (1.2)$$

In order to evaluate the pion content of each bin in data, we scale the measured bin by the corresponding relative pion content found in MC, as follows

$$N_{\text{Int}}^{\pi \text{RecoData}} = N_{\text{Int}}^{\text{TOTData}}(E_i) - B_{\text{Int}}^{\text{Data}}(E_i) = C_{\text{Int}}^{\pi MC}(E_i) N_{\text{Int}}^{\text{TOTData}}(E_i). \quad (1.3)$$

The pion content is evaluated separately in the interacting and incident histograms. Their ratio determines a correction to the measured raw cross section. For example, the measured raw cross section of a sample with enhanced muons content will tend to be lower than the raw cross section of a muon free sample. This is because most of the muons will cross the TPC without stopping, thus contributing almost exclusively to the incident histogram, forcing the pion content to be lower in the incident histogram than in the interacting; thus, the correction will tend to enhance the cross section.

1.4 Estimate of Energy Loss before the TPC

The beamline particles travel a path from where their momentum is measured in the beamline until they are tracked again inside the TPC. In the LArIAT geometry, a particle leaving the WC4 will encounter the materials listed in Table 1.4 before being registered again. The energy lost by the particle in this non-instrumented material modifies the particle’s kinetic energy and directly affects the cross section measurement, as shown in equation 5.

Material	density [g/cm ³]	width [cm]
Fiberglass laminate (G10)	1.7	1.28
Liquid Argon	1.4	3.20
Stainless Steel	7.7	0.23
Titanium	4.5	0.04
Air	$1.2 \cdot 10^{-3}$	89.43
Plastic Scintillator	1.03	1.20 (+ 1.30)

Table 1.4: LArIAT material budget from WC4 to the TPC Front Face.

We derive an estimate of the energy loss between the beamline momentum measurement and the TPC (E_{loss}) from the pion and kaon DDMC samples, since this quantity is not measurable directly on data. The E_{loss} distribution for the 60A and 100A pion sample is shown in figure 1.10, left and right respectively. A clear double peaked structure is visible, which is due to the particles either missing or hitting the HALO paddle: a schematic rendering of this occurrence is shown in figure 1.11. The kinematic at WC4 determines the trajectory of a particle and whether or not it will hit the halo paddle. In figure 1.12, we plot the true horizontal component of the momentum P_x versus the true X position at WC4 for pions missing the halo paddle (left) and for pions hitting the halo paddle (right) for the 60A MC simulation runs – analogous plots are obtained with the 100A simulation. These distributions can be separated drawing a line in this position-momentum space. We use a logistic regression [13] as a classifier to find the best separating line, shown in both plots as the red

line. We classify as “hitting the halo paddle” all pions whose P_x and X are such that

$$P_x + 0.02 * X - 0.4 < 0$$

and as “missing the halo paddle” all pions whose P_x and X are such that

$$P_x + 0.02 * X - 0.4 > 0,$$

543 where the coefficients of the line are empirically found by the logistic regression es-
 544 timation. Overall, this simple method classifies in the right category (hit or miss)
 545 about 86% of the pion events. In MC, we assign $E_{loss} = 32 \pm 4$ MeV for pion events
 546 classified as “hitting the halo paddle”; we assign $E_{loss} = 24 \pm 3$ MeV for pion events
 547 classified as “missing the halo paddle”. We apply the same classifier on data. A
 548 scan of the simulated geometry showed an excess of 3 cm of uninstrumented argon
 549 compared with the surveyed detector geometry. We account for this difference by
 550 assigning in data $E_{loss} = 24 \pm 6$ MeV for pion events classified as “hitting the halo
 551 paddle” and $E_{loss} = 17 \pm 6$ MeV for pion events classified as “missing the halo pad-
 552 dle”, where the uncertainty is derived as the standard deviation of the double peaked
 553 distribution.

554 The summary of the values for used for E_{Loss} for the pion sample is listed in table
 555 1.5 with the analogous results for the study on the kaon case.

	E_{loss} [MeV]	
	Hitting Halo	Missing Halo
Pion MC	32 ± 4	24 ± 3
Pion Data	25 ± 6	17 ± 6
Kaon MC	37 ± 5	31 ± 4
Kaon Data	26 ± 6	22 ± 6

Table 1.5: Energy loss for pions and kaons.

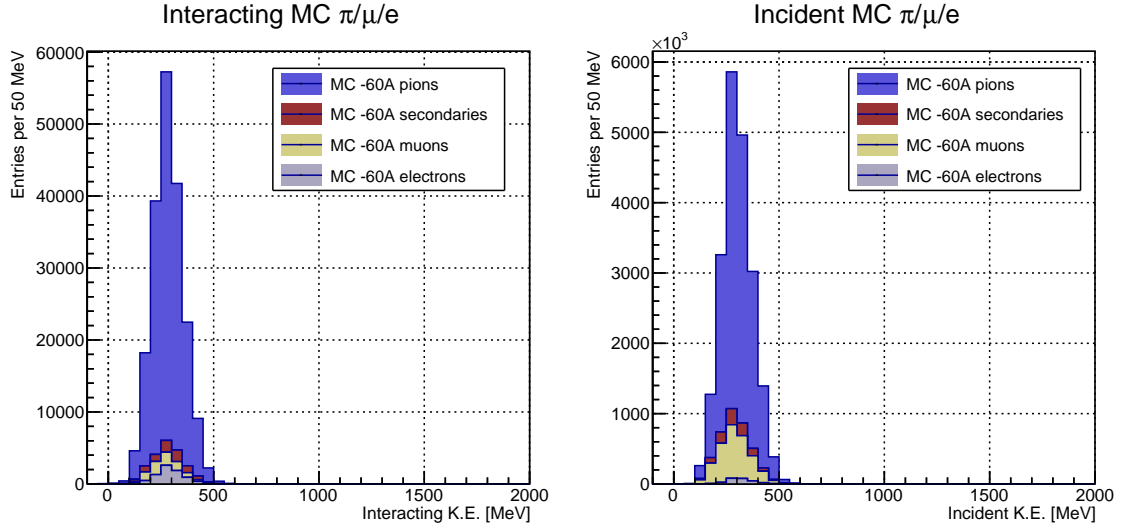


Figure 1.9: Left: staggered contributions to the interacting kinetic energy distribution for electron (grey), muons (yellow) and pion (blue) in the 60A simulation sample. Right: staggered contributions to the incident kinetic energy distribution for electron (grey), muons (yellow) and pion (blue) in the 60A simulation sample.

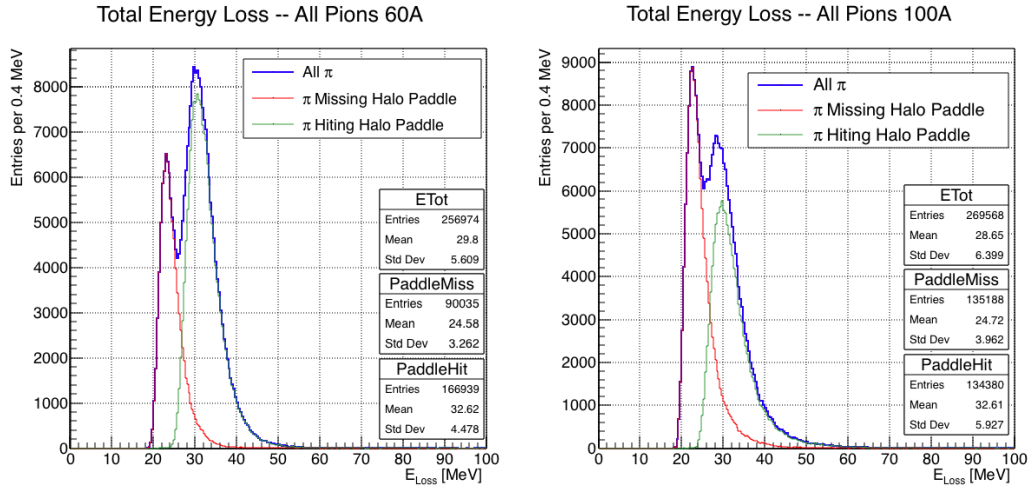


Figure 1.10: True energy loss between WC4 and the TPC front face according to the MC simulation of negative pions of the 60A runs (left) and of the 100A runs (right). The distribution for the whole data sample is shown in blue, the distribution for the pions missing the halo is shown in red, and the distribution for the pions hitting the halo is shown in green.

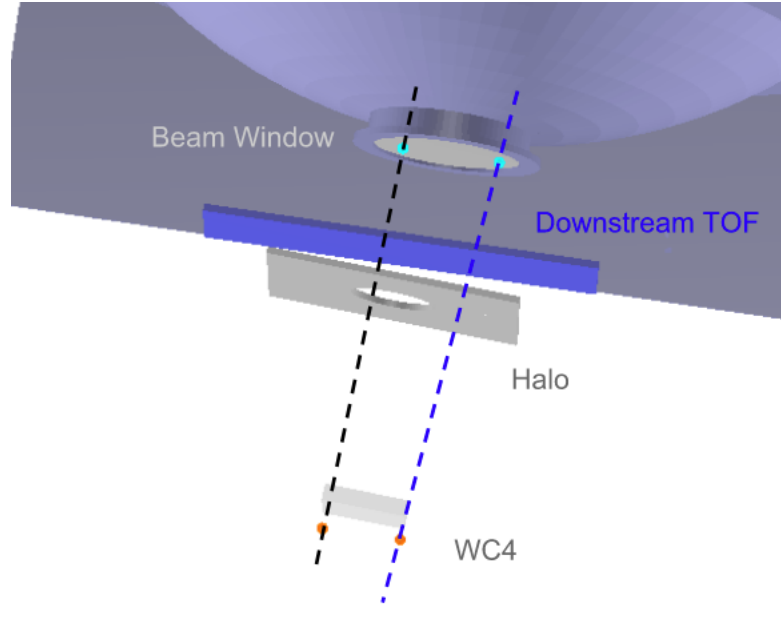


Figure 1.11: Schematic rendering of the particle path between WC4 and the TPC front face. The paddle with the hollow central circle represents the Halo paddle. We illustrate two possible trajectories: in black, a trajectory that miss the paddle and goes through the hole in the Halo, in blue a trajectory that hits the Halo paddle and goes through the scintillation material.

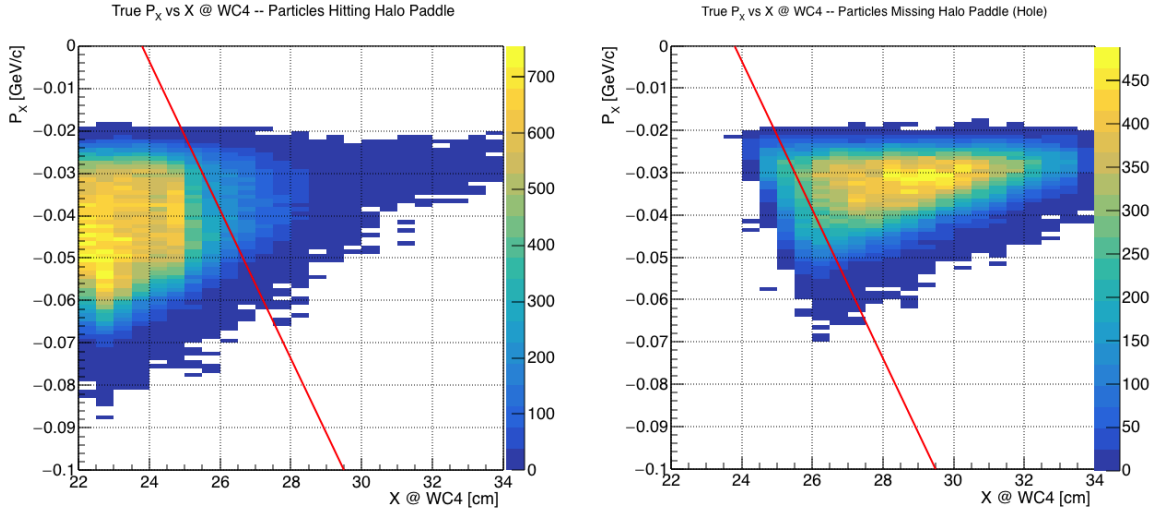


Figure 1.12: Horizontal component of the true momentum vs the horizontal position at WC4 for MC simulated pions of the 60A runs. The plot on the left shows the distribution for pion that miss the halo paddle and the plot on the right shows the distributions for pions that hit the halo. The form of the classifier is overlaid to both plots (red line).

1.5 Tracking Studies

In this section, we describe three studies. The first is a justification of the selection criteria for the beamline handshake with the TPC information. We perform this study to boost the correct identification of the particles in the TPC associated with the beamline information, while maintaining sufficient statistics for the cross section measurement. The second study is an optimization of the tracking algorithm, with the scope of maximizing the identification of the hadronic interaction point inside the TPC. These two studies are related, since the optimization of the tracking is performed on TPC tracks which have been matched to the wire chamber track; in turn, the tracking algorithm for TPC tracks determines the number of reconstructed tracks in each event used to try the matching with the wire chamber track. Starting with a sensible tracking reconstruction, we perform the WC2TPC matching optimization first, then the tracking optimization. The WC2TPC match purity and efficiency are then calculated again with the optimized tracking.

The third study is an evaluation of the angular resolution of the tracking algorithm in data and MC, which is particularly important in the context of the cross section analyses.

1.5.1 Study of WC to TPC Match

Plots I want in this section:

1. WC2TPC MC DeltaX, DeltaY and α

Scope of this study is assessing the goodness of the wire chamber to TPC match on Monte Carlo and decide the selection values we will use on data. A word of caution is necessary here. With this study, we want to minimize pathologies associated with the presence of the primary hadron itself, e.g. the incorrect association between the

580 beamline hadron and its decay products inside the TPC. Assessing the contamination
 581 from pile-up³, albeit related, is beyond the scope of this study.

582 In MC, we are able to define a correct WC2TPC match using the Geant4 truth
 583 information. We are thus able to count how many times the WC tracks is associated
 584 with the wrong TPC reconstructed track.

585 We define a correct match if the all following conditions are met:

- 586 - the length of the true primary Geant4 track in the TPC is greater than 2 cm,
- 587 - the length of the reconstructed track length is greater than 2 cm,
- 588 - the Z position of the first reconstructed point is within 2 cm from the TPC
 589 front face
- 590 - the distance between the reconstructed track and the true entering point is the
 591 minimum compared with all the other reconstructed tracks.

592 In order to count the wrong matches, we consider all the reconstructed tracks
 593 whose Z position of the first reconstructed point lies within 2 cm from the TPC front
 594 face. Events with true length in TPC < 2 cm are included. Since hadrons are shot
 595 100 cm upstream from the TPC front face, the following two scenarios are possible
 596 from a truth standpoint:

- 597 [*Ta*] the primary hadron decays or interact strongly before getting to the TPC,
- 598 [*Tb*] the primary hadron enters the TPC.

599 As described in Section 0.2, we define a WC2TPC match according to the relative
 600 position of the WC and TPC track parametrized with ΔR and the angle between

3. We remind the reader that the DDMC is a single particle Monte Carlo, where the beam pile up is not simulated.

601 them, parametrized with α . Once we choose the selection values r_T and α_T to de-
 602 termine a reconstructed WC2TPC match, the following five scenarios are possible in
 603 the truth to reconstruction interplay :

- 604 1) only the correct track is matched
- 605 2) only one wrong track is matched
- 606 3) the correct track and one (or more) wrong tracks are matched
- 607 4) multiple wrong tracks matched.
- 608 5) no reconstructed tracks are matched

609 Since we keep only events with one and only one match, we discard cases 3), 4)
 610 and 5) from the events used in the cross section measurement. For each set of r_T and
 611 α_T selection value, we define purity and efficiency of the selection as follows:

$$\text{Efficiency} = \frac{\text{Number of events correctly matched}}{\text{Number of events with primary in TPC}}, \quad (1.4)$$

$$\text{Purity} = \frac{\text{Number of events correctly matched}}{\text{Total number of matched events}}. \quad (1.5)$$

612 Figure 1.13 shows the efficiency (left) and purity (right) for WC2TPC match as
 613 a function of the radius, r_T , and angle, α_T , selection value. It is apparent how both
 614 efficiency and purity are fairly flat as a function of the radius selection value at a
 615 given angle. This is not surprising. Since we are studying a single particle gun Monte
 616 Carlo sample, the wrong matches can occur only for mis-tracking of the primary or
 617 for association with decay products; decay products will tend to be produced at large
 618 angles compared to the primary, but could be fairly close to the in x and y projection
 619 of the primary. The radius cut would play a key role in removing pile up events.

For LArIAT cross section measurements, we generally prefer purity over efficiency, since a sample of particles of a pure species will lead to a better measurement. Obviously, purity should be balanced with a sensible efficiency to avoid rejecting the whole sample.

We choose $(\alpha_T, r_T) = (8 \text{ deg}, 4 \text{ cm})$ and get a MC 85% efficiency and 98% purity for the kaon sample and a MC 95% efficiency and 90% purity for the pion sample.

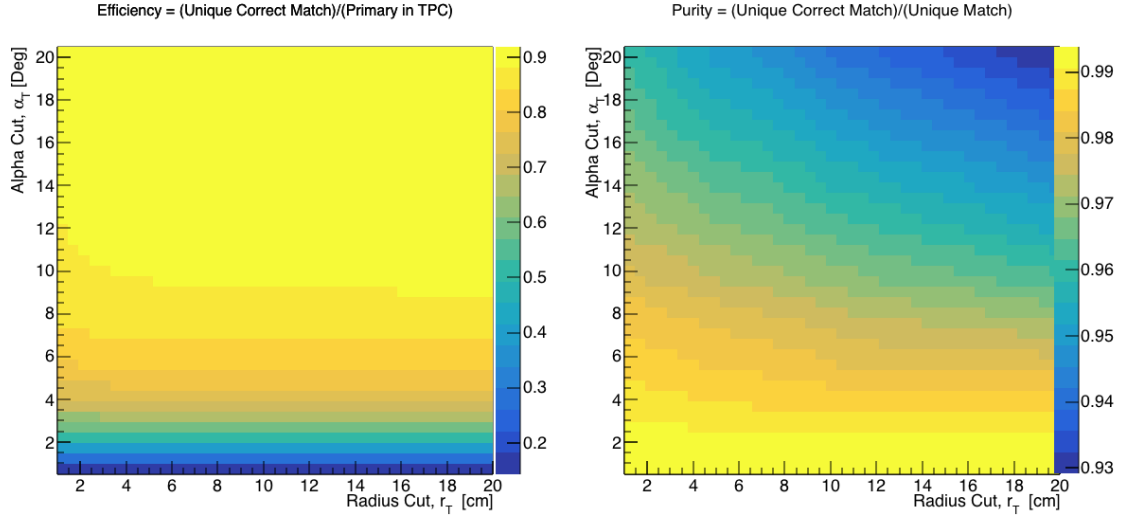


Figure 1.13: Efficiency (left) and purity (right) for WC2TPC match as a function of the radius and angle selections for the kaon sample.

1.5.2 Tracking Optimization

1.5.3 Angular Resolution

Scope of this study is to understand and compare the tracking performances and angular resolution of the TPC tracking on data and MC. We use the angular resolution of the tracking to determine the value of smallest angle that we can reconstruct with a non-zero efficiency, effectively determining a selection on the angular distribution of the cross section measurement due to the tracking performance. This study is performed on the pion sample, but its results are extrapolated to the kaon case.

634 We start by selecting all the WC2TPC matched tracks used for the cross section
635 analysis. These tracks can contain from a minimum of 3 3D-space points to a maxi-
636 mum of 240 3D-space points. We fit a line to all the 3D-space points associated with
637 the track. For each track we calculate the average distance between each point in
638 space and the fit line as follows

$$\bar{d} = \frac{\sum_i^N d_i}{N}, \quad (1.6)$$

639 where N is the number of 3D-space points of the track and d_i is the distance of the
640 i -th space point to the line fit. Several tests to compare the goodness of fit between
641 data and MC have been considered. We decided to use \bar{d} for its straightforward
642 interpretation. The \bar{d} distribution for data and MC is shown in Figure 1.14 and
643 shows a relatively good agreement between data and MC.

644 A visual representation of the procedure used to evaluate the angular resolution is
645 shown in Figure 1.16. For each track, we order the space points according to their Z
646 position along the positive beam direction (panel a) and we split them in two sets: the
647 first set contains all the points belonging to the first half of the track and the second
648 set contains all the points belonging the second half of the track. We remove the last
649 four points in the first set and the first four points in the second set, so to have a
650 gap in the middle of the original track (panel b). We fit the first and the second set
651 of points with two lines (panel c). We then calculate the angle between the fit of the
652 first and second half α (panel d). The angle α determines the spatial resolution of
653 the tracking. The distributions for data and MC for α are given in Figure 1.15. The
654 mean of the data and MC angular resolution are respectively

$$\bar{\alpha}_{Data} = (5.0 \pm 4.5) \text{ deg}, \quad (1.7)$$

$$\bar{\alpha}_{MC} = (4.5 \pm 3.9) \text{ deg}. \quad (1.8)$$

Interaction angles smaller than the angle resolution are indistinguishable for the reconstruction. Therefore, we assess our ability to measure the cross section to be limited to interaction angles greater than 5.0 deg. More accurate studies of the angular resolution as a function of the kinetic energy and track length, albeit interesting, are left for an improvement of the analysis.

It is beneficial to take a moment to describe the definition of interaction angle. In case of elastic scattering, the definition is straightforward: the interaction angle is the angle between the incoming and outgoing pion, i.e.

$$\theta = \cos^{-1} \left(\frac{\vec{p}_{\text{incoming}} \cdot \vec{p}_{\text{outgoing}}}{|\vec{p}_{\text{incoming}}| |\vec{p}_{\text{outgoing}}|} \right). \quad (1.9)$$

In case of inelastic scattering, the presence of several topologies requires a more complex definition, as shown in figure 1.17. We define the scattering angle as the biggest of the angles between the incoming pion and the visible daughters, where the visible daughters are charged particles that travel more than 0.47 cm in the detector (see panel a); in case all the daughters are invisible, the angle is assigned to be 90 deg (see panel b). We chose this working definition of scattering angle for inelastic scattering keeping in mind how our tracking reconstruction works: the tracking will stop correctly in case of all the daughters are not visible in the detector and it is likely to stop correctly if multiple daughters form an interaction vertex. The only “dangerous” case is the production of one charged daughter plus neutrals, which we can study with this working definition of scattering angle (see panel c).

We can see the effects of the angular resolution on the cross section by plotting the true Geant4 cross section for interaction angles greater than a minimum interaction angle. Figure 1.18 shows the true Geant4 cross section for interaction angles greater than 0 deg (green), 4.5 deg (red), 5.0 deg (blue) and 9.0 deg (yellow). A small 0.5 deg systematic shift between the mean of the data and MC angular resolution is present.

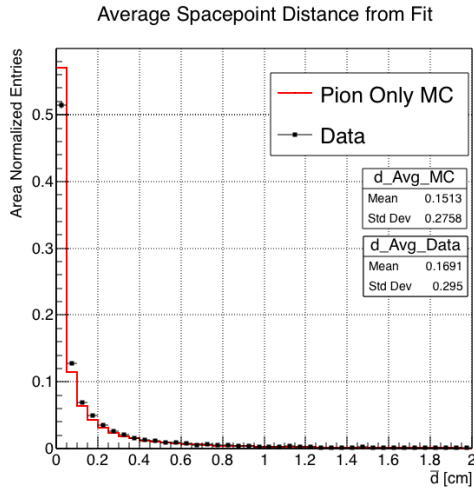


Figure 1.14: Distributions of the average distance between each 3D point in space and the fit line, \bar{d} for the data used in the pion cross section analysis and the pion only DDMC. The distributions are area normalized.

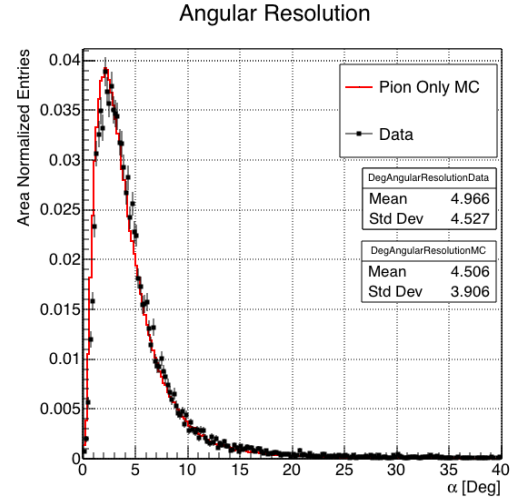


Figure 1.15: Distributions of angular resolution α for data used in the pion cross section analysis and pion only DDMC. The distributions are area normalized.

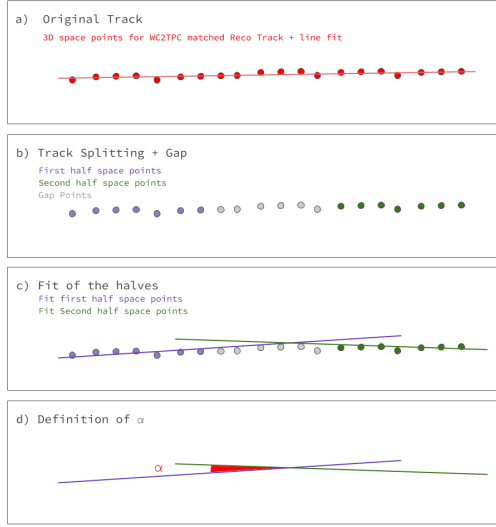


Figure 1.16: A visual representation of the procedure used to evaluate the angular resolution.

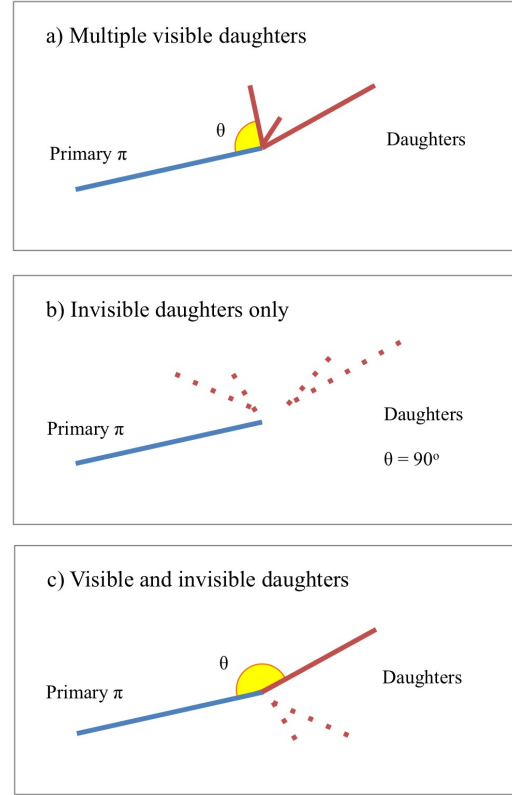


Figure 1.17: A visual representation of the scattering angle definition in case of inelastic scattering.

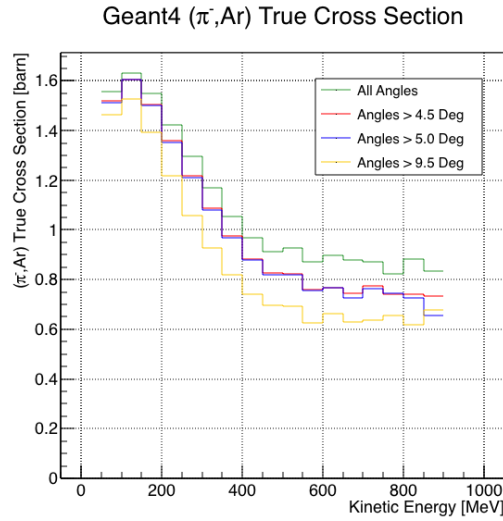


Figure 1.18: True (π^- , Ar) cross section for interaction angles greater than 0 deg (green), 4.5 deg (red), 5.0 deg (blue) and 9.0 deg (yellow).

1.6 Calorimetry Studies

The ability to measure the kinetic energy of hadrons in the TPC is fundamental for the cross section analyses. Thus, we describe first how we calibrate the TPC calorimetric response (Section 1.6.1) and how we measure the kinetic energy of the hadrons in the TPC (Section 1.6.2).

1.6.1 Energy Calibration

Scope of the energy calibration is to identify the factors which convert the charge collected (dQ) to energy deposited in the chamber (dE). As described in section ??, this is a multi-step procedure. In LArIAT, we first correct the raw charge by the electronic noise on the considered wire [102], then by the electron lifetime [103], and then by the recombination using the ArgoNeut recombination values. Lastly, we apply overall calibration of the energy, i.e. we determine the “calorimetry constants” using the procedure described in this section.

We independently determine the calorimetry constants for Data and Monte Carlo in the LArIAT Run-II Data samples using a parametrization of the stopping power (a.k.a. energy deposited per unit length, dE/dX) as a function of momentum. This is done by comparing the stopping power measured on reconstructed quantities against the Bethe-Bloch theoretical prediction for various particle species (see Equation ??). We obtain the theoretical expectation for the dE/dX most probable value of pions (π), muons (μ), kaons (K), and protons (p) in the momentum range most relevant for LArIAT (Figure 1.19) using the tables provided by the Particle Data Group [100] for liquid argon [1].

The basic idea of this calibration technique is to utilize a sample of beamline events with known particle species and momentum to measure the dE/dX of the corresponding tracks in the TPC. In particular, we decided to use positive pions as

704 calibration sample and samples from all the other particle species as cross check. Once
 705 the dE/dX of the positive pion sample has been measured at various momenta, we
 706 tune to calorimetry constants within the reconstruction software to align the measured
 707 values to match the theoretical ones found in Figure 1.19.

708 In data, we start by selecting a sample of beamline positive pion beamline can-
 709 didates without any restriction on their measured momentum⁴. We then apply the
 710 WC2TPC match and subtract the energy loss upstream to the TPC front face, de-
 711 termining the momentum at the TPC front face. For each surviving pion candidate,
 712 we measure the dE/dx at each of the first 12 spacepoints associated the 3D recon-
 713 structed track, corresponding to a ~ 5 cm portion. These dE/dX measurements are
 714 then put into a histogram that corresponds to measured momentum of the track.
 715 The dE/dX histograms are sampled every 50 MeV/c in momentum (e.g. 150 MeV/c
 716 $< P < 200$ MeV/c, 200 MeV/c $< P < 250$ MeV, etc...). This process of selecting,
 717 sampling, and recording the dE/dX for various momentum bins is repeated over the
 718 entire sample of events, allowing us to collect sufficient statistic in most of the mo-
 719 mentum bins between 150 MeV/c and 1100 MeV/c. On average, pions and muons
 720 only lose ~ 10 MeV in this 5 cm section of the track and protons lose ~ 20 MeV. Thus
 721 choosing 50 MeV/c size bins for our histograms covers the energy spread within those
 722 bins due to energy loss from ionization for all the particle species identifiable in the
 723 beamline. Each 50 MeV/c momentum binned dE/dX histogram is now fit with a
 724 simple Landau function. The most probable value (MPV) and the associated error
 725 on the MPV from the fit are extracted and plotted against the theoretical prediction
 726 Figure 1.19. Depending on the outcome of the data-prediction comparison, we modify
 727 the calorimetry constants and we repeat the procedure until a qualitative agreement
 728 is achieved. We perform this tuning for the collection and induction plane separately.
 729 As a cross check to the calorimetry constants determined using the positive pions,

4. it should be noted that some muon and positron contamination is present in the π^+ sample

we lock the constants and plot the dE/dx versus momentum distribution of all the other particle species identifiable in the beamline data ($\pi/\mu/e$, K , p, in both polarities) against the corresponding Beth-Bloch prediction. The agreement between data from the other particle species and the predictions is the expected result of this cross check. The results of the tuning and cross check for Run-II data on the collection plane is shown in Figure 1.20 negative polarity data on top, positive polarity data on the bottom.

In MC, we simulate the corresponding positive pion sample with the DDMC (see section 1.2.2) and follow the same steps as in data. More details on the calorimetry tuning can be found in [78].

Add agreement between data and MC for dedx for pions

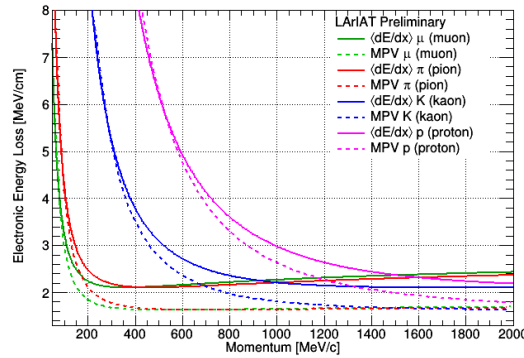


Figure 1.19: Stopping power for pions, muons, kaons, and protons in liquid argon over the momentum range most relevant for LArIAT according to the Beth-Bloch equation. The solid lines represent the prediction for the mean energy dE/dX , while the dashed lines are the predictions for the MPV.

1.6.2 Kinetic Energy Measurement

The measured kinetic energy of a hadron candidate at each argon slab determines which bins of the interacting and incident histograms a selected event is going to fill. In this section, we define the measurement on the kinetic energy and determine the related uncertainty. We will propagate this uncertainty into the cross section

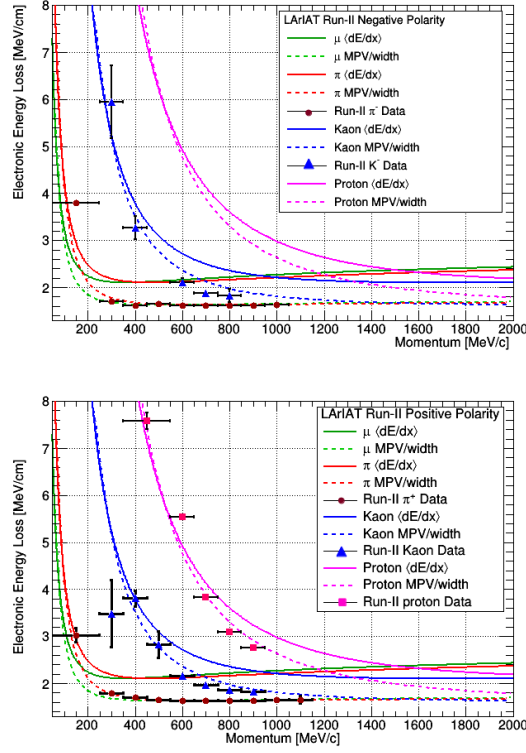


Figure 1.20: Stopping power versus Momentum for Run-II negative (top) and positive (bottom) polarity data. We achieve the agreement between the Bethe-Bloch predictions and the distribution obtained with of the positive pions (top plot, red dots) by tuning the calorimetry constants. Once the calorimetry constants are locked in, the agreement between the other particle species and the Bethe-Bloch predictions follows naturally.

746 measurement, as discussed in Section 2.1.2 for the pion cross section and in Section
747 ?? for the kaon cross section.

748 The kinetic energy of a hadron at the j^{th} slice of argon in the TPC is given by

$$KE_j = \sqrt{p_{\text{Beam}}^2 + m_{\text{Beam}}^2} - m_{\text{Beam}} - E_{\text{Loss}} - E_{\text{FF-j}}, \quad (1.10)$$

749 where p_{Beam} is the momentum measured by the beamline detectors, m_{Beam} is the
750 mass of the hadron as reported in the PDG, E_{Loss} is the energy loss between the
751 beamline and the TPC, and $E_{\text{FF-j}}$ is the energy that the hadron deposited from the

752 TPC front face until the j^{th} slice. The uncertainty on KE_j is then given by

$$\delta KE_j = \sqrt{\delta p_{Beam}^2 + \delta E_{Loss}^2 + \delta E_{\text{dep FF-j}}^2}, \quad (1.11)$$

753 where we have dropped the uncertainty on the mass, since it is orders of magnitude
 754 smaller than the other uncertainties. We assume the relative uncertainty on p_{Beam} to
 755 be 2%, and the uncertainty on the energy loss upstream to be 7 MeV, as calculated
 756 in Section 1.4. We describe the estimate of the uncertainty on $E_{\text{FF-j}}$ in the rest of
 757 this section.

758 The energy deposited by the hadron from the TPC front face until the j^{th} slice is
 759 the sum of the measured energy deposited in each previous slabs E_i , i.e.

$$E_{\text{FF-j}} = \sum_{i < j} E_i, \quad (1.12)$$

760 where E_i is measured in each slab as the product of the stopping power, dE/dX_i ,
 761 and the track pitch, $Pitch_i$, for that point. If we assume conservatively that the
 762 measurements of E_i are not independent from one another, the uncertainty on $E_{\text{FF-j}}$
 763 becomes

$$\delta E_{\text{FF-j}} = (j - 1)\delta E_i, \quad (1.13)$$

764 where δE_i is the uncertainty on the energy loss in one slab of argon.

765 The left side of Figure 1.21 shows the distribution of the energy deposited in each
 766 slab of argon, for the 60A negative pion dataset in black and for the pion only MC
 767 in blue. The analogous plot for the -100A negative pion data set is show on the right
 768 side of Figure 1.21. The distributions are fitted with a landau displayed in red for
 769 data and in teal for MC. The uncertainty on E_i is given by the width of the Landau
 770 fit to the data. A small systematic uncertainty is given by a 1.0% difference between
 771 the most probable value of the landau fits in data and MC.

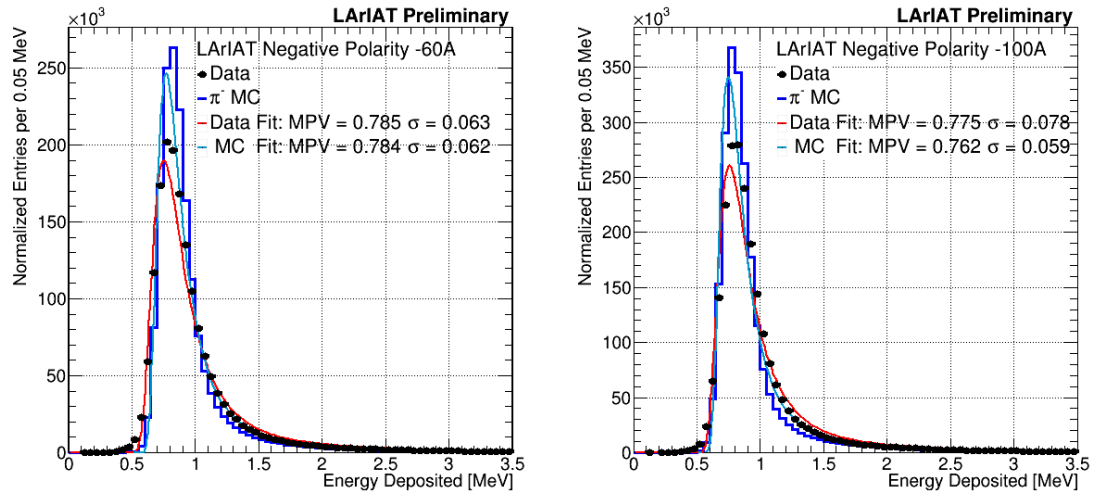


Figure 1.21: Energy deposited E_i in a single slab of argon for the pion -60A runs (left) and -100A runs (right). The data is shown in black, the MC in blue. The distributions are fitted with a landau displayed in red for data and in teal for MC.

Chapter 2

Negative Pion Cross Section Measurement

In this chapter, we show the result of the thin slice method to measure the (π^- -Ar) total hadronic cross section. In Section 2.1, we start by measuring the raw cross section, i.e. the cross section obtained exclusively using data reconstruction, without any additional corrections. In Section 2.2, we apply a statistical subtraction of the background contributions based on simulation and a correction for detection inefficiency. The final results are presented in Section 2.3.

2.1 Raw Cross Section

We measure the raw (π^- -Ar) total hadronic cross section as a function of the kinetic energy in the two chosen data sets, the -60A and -100A negative runs. As we will clarify in Section 2.2, the corrections to the raw cross section depend on the beam conditions and need to be calculated independently for the two datasets. Thus, we present here the measurement of the raw cross section on the two datasets separately.

787 As stated in section 0.3.2, the raw cross section is given by the equation

$$\sigma_{TOT}(E_i) = \frac{1}{n\delta X} \frac{N_{Int}^{TOT}(E_i)}{N_{Inc}^{TOT}(E_i)}, \quad (2.1)$$

788 where N_{Int}^{TOT} is the measured number of particles interacting at kinetic energy E_i ,
 789 N_{Inc}^{TOT} is the measured number of particles incident on an argon slice at kinetic energy
 790 E_i , n is the density of the target centers and δX is the thickness of the argon slice.
 791 The density of the target centers and the slab thickness are $n = 0.021 \cdot 10^{24} \text{ cm}^{-3}$ and
 792 $\delta X = 0.47 \text{ cm}$, respectively.

793 Figure 2.1 shows the distribution of N_{Int}^{TOT} as a function of the kinetic energy for
 794 the 60A dataset on the left and for the 100A dataset on the right. The data central
 795 points are represented by black dots, the statistical uncertainty is shown in black,
 796 while the systematic uncertainty is shown in red. Data is displayed over the N_{Int}^{TOT}
 797 distribution obtained with a MC mixed sample of pions, muon and electrons (addi-
 798 tional details on the composition will be provided in Section ??). The contribution
 799 from the simulated pions is shown in blue, the one from secondaries in red, the one
 800 from muons in yellow and the ones from electrons in gray. The simulated pion's and
 801 backgrounds' contributions are stacked; the sum of the integrals from each particle
 802 species is normalized to the integral of the data.

803 Figure 2.2 shows the distribution of N_{Inc}^{TOT} for the 60A dataset on the left and for
 804 the 100A dataset on the right. Data is displayed over the MC. The same color scheme
 805 and normalization procedure is used for both the interacting and incident histograms.

806 Figure 2.3 shows the raw cross section for the 60A dataset on the left and for the
 807 100A dataset on the right, statistical uncertainty in black and systematic uncertainty
 808 in red. The raw data cross section is overlaid to the reconstructed cross section for
 809 the MC mixed sample, displayed in azure. Since the background contributions and
 810 the detector effects for the 60A and 100A sample are different, it is premature to

811 compare the raw cross sections obtained from the two samples at this point.

812 We describe the calculation of the statistical uncertainty for the interacting, in-
 813 cident and cross section distributions in Section 2.1.1; we describe the procedure to
 814 calculate the corresponding systematics uncertainty on Section 2.1.2.

815 2.1.1 Statistical Uncertainty

816 The statistical uncertainty for a given kinetic energy bin of the cross section is cal-
 817 culated by error propagation from the statistical uncertainty on $N_{\text{Inc}}^{\text{TOT}}$ and $N_{\text{Int}}^{\text{TOT}}$
 818 correspondent bin. Since the number of incident particles in each energy bin is given
 819 by a simple counting, we assume that $N_{\text{Inc}}^{\text{TOT}}$ is distributed as a poissonian with mean
 820 and variance equal to $N_{\text{Inc}}^{\text{TOT}}$ in each bin. On the other hand, $N_{\text{Int}}^{\text{TOT}}$ follows a bino-
 821 mial distribution: a particle in a given energy bin might or might not interact. The
 822 variance for the binomial is given by

$$\text{Var}[N_{\text{Int}}^{\text{TOT}}] = \mathcal{N} P_{\text{Interacting}} (1 - P_{\text{Interacting}}). \quad (2.2)$$

823 Since the interaction probability $P_{\text{Interacting}}$ is $\frac{N_{\text{Int}}^{\text{TOT}}}{N_{\text{Inc}}^{\text{TOT}}}$ and the number of tries \mathcal{N} is
 824 $N_{\text{Inc}}^{\text{TOT}}$, equation 2.2 translates into

$$\text{Var}[N_{\text{Int}}^{\text{TOT}}] = N_{\text{Inc}}^{\text{TOT}} \frac{N_{\text{Int}}^{\text{TOT}}}{N_{\text{Inc}}^{\text{TOT}}} (1 - \frac{N_{\text{Int}}^{\text{TOT}}}{N_{\text{Inc}}^{\text{TOT}}}) = N_{\text{Int}}^{\text{TOT}} (1 - \frac{N_{\text{Int}}^{\text{TOT}}}{N_{\text{Inc}}^{\text{TOT}}}). \quad (2.3)$$

825 $N_{\text{Inc}}^{\text{TOT}}$ and $N_{\text{Int}}^{\text{TOT}}$ are not independent. The statistical uncertainty on the cross
 826 section is thus calculated as

$$\delta\sigma_{TOT}(E) = \sigma_{TOT}(E) \left(\frac{\delta N_{\text{Int}}^{\text{TOT}}}{N_{\text{Int}}^{\text{TOT}}} + \frac{\delta N_{\text{Inc}}^{\text{TOT}}}{N_{\text{Inc}}^{\text{TOT}}} \right) \quad (2.4)$$

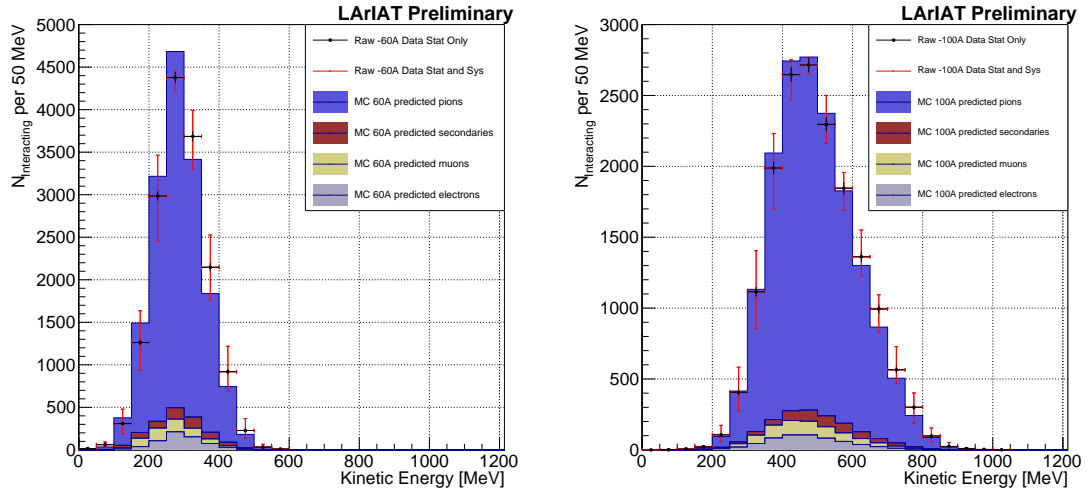


Figure 2.1: Raw number of interacting pion candidates as a function of the reconstructed kinetic energy for the 60A runs (left) and for the 100A runs (right). The statistical uncertainties are shown in black, the systematic uncertainties in red.

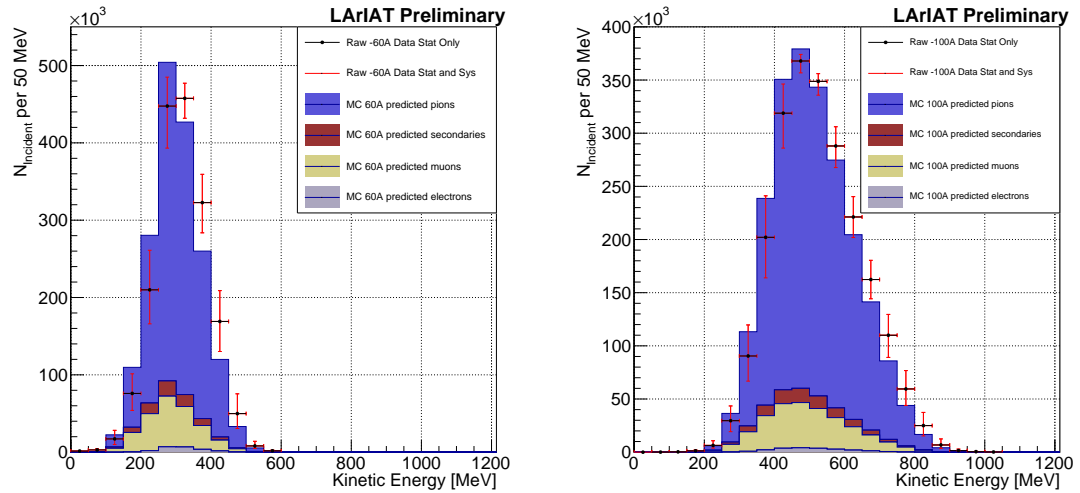


Figure 2.2: Raw number of incident pion candidates as a function of the reconstructed kinetic energy for the 60A runs (left) and for the 100A runs (right). The statistical uncertainty is shown in black, the systematic uncertainties in red.

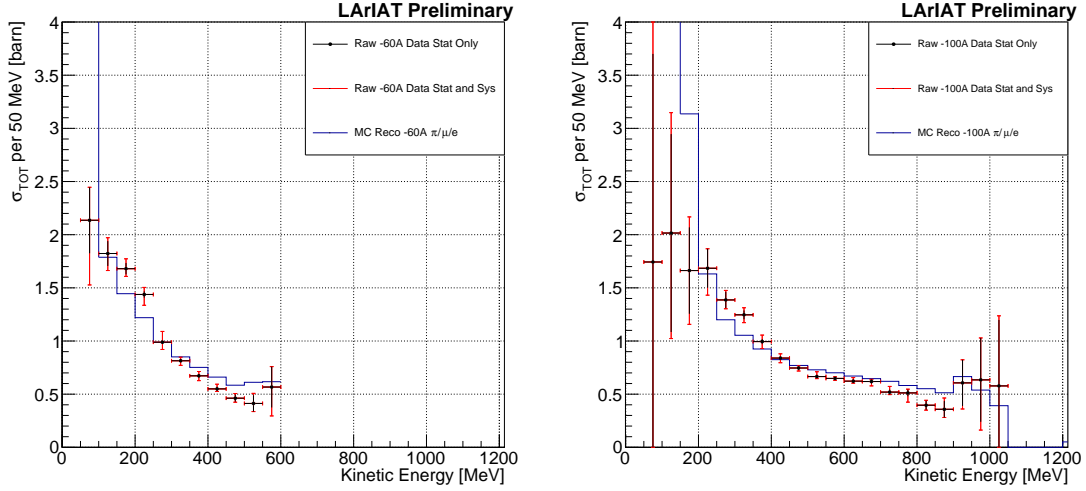


Figure 2.3: Raw (π^- -Ar) total hadronic cross section for the 60A runs (left) and for the 100A runs (right). The statistical uncertainty is shown in black, the systematic uncertainties in red. The raw cross section obtained with a MC mixed sample of pions, muon and electrons in the percentage predicted by G4Beamline is shown in azure.

827 where:

$$\delta N_{\text{Inc}}^{\text{TOT}} = \sqrt{N_{\text{Inc}}^{\text{TOT}}} \quad (2.5)$$

$$\delta N_{\text{Int}}^{\text{TOT}} = \sqrt{N_{\text{Int}}^{\text{TOT}} \left(1 - \frac{N_{\text{Int}}^{\text{TOT}}}{N_{\text{Inc}}^{\text{TOT}}} \right)}. \quad (2.6)$$

828 2.1.2 Treatment of Systematics

829 The only systematic effect considered in the measurement of the raw cross section
830 results from the propagation of the uncertainty associate with the measurement of
831 the kinetic energy at each argon slab. As shown in Section 1.6.2, the uncertainty on
832 the kinetic energy of a pion candidate at the j^{th} slab of argon is given by

$$\delta KE_j = \sqrt{\delta p_{\text{Beam}}^2 + \delta E_{\text{Loss}}^2 + \delta E_{\text{dep FF-j}}^2} \quad (2.7)$$

$$= \sqrt{(2\% p_{\text{Beam}})^2 + (\sim 6 \text{ [MeV]})^2 + (j-1)^2 (\sim 0.08 \text{ [MeV]})^2}. \quad (2.8)$$

833 We propagate this uncertainty by varying the energy measurement KE_j at each
834 argon slab. We measure $N_{\text{Inc}}^{\text{TOT}}$, $N_{\text{Int}}^{\text{TOT}}$ and the cross section in three cases: first
835 assigning the measured KE_j at each kinetic energy sampling, then assigning $KE_j +$
836 δKE_j , and finally assigning $KE_j - \delta KE_j$. The difference between the values obtained
837 using the KE_j sampling and the maximum and minimum values in each kinetic energy
838 bin determines the systematic uncertainty.

839 2.2 Corrections to the Raw Cross Section

840 As described in section 0.3.3, we need to apply a background correction and an
841 efficiency correction in order to derive the true pion cross section from the raw cross
842 section. The true cross section is given in equation 9,

$$\sigma_{TOT}^{\pi^-}(E_i) = \frac{1}{n\delta X} \frac{\epsilon^{\text{Inc}}(E_i)}{\epsilon^{\text{Int}}(E_i)} \frac{C_{\text{Int}}^{\pi MC}(E_i)}{C_{\text{Inc}}^{\pi MC}(E_i)} \frac{N_{\text{Int}}^{\text{TOT}}(E_i)}{N_{\text{Inc}}^{\text{TOT}}(E_i)}. \quad (9)$$

843 Section 2.2.1 describes the evaluation of pion content in the interacting and inci-
844 dent histograms, ($C_{\text{Int}}^{\pi MC}(E_i)$ and $C_{\text{Inc}}^{\pi MC}(E_i)$) and the propagation to the cross section
845 measurement of the relative systematic uncertainties.

846 Section 2.2.2 describes the procedure employed to obtain the efficiency corrections
847 $\epsilon^{\text{Int}}(E_i)$ and $\epsilon^{\text{Inc}}(E_i)$ and the propagation to the cross section measurement of the
848 relative uncertainties.

849 2.2.1 Background subtraction

850 We use the procedure described in 1.3.2 to evaluate the relative pion content in
851 the interacting histogram $C_{\text{Int}}^{\pi MC}(E_i)$ and the relative pion content in the incident
852 $C_{\text{Inc}}^{\pi MC}(E_i)$. We start by evaluating the relative pion content assuming the beamline
853 composition simulated by G4Beamline, whose pion, muon and electron percentages
854 per beam condition are reported again in the first line of Table 2.1. The left side of

Figure 2.4 shows the MC estimated relative pion content for the interacting histogram as function of kinetic energy for the 60A runs (top) and 100A runs (bottom). The right side of the same figure shows the MC estimated relative pion content for the incident histogram as function of kinetic energy for the 60A runs (top) and 100A runs (bottom). In Figure 2.4 the central curves displayed in light blue are obtained using the beamline composition as predicted by G4Beamline: these are the correction curves for the relative pion content applied to data.

So, the question now becomes: how well do we know the beamline composition? In absence of additional data constraints, we take a 100% systematic uncertainty on the electron content, reported in lines 3 and 4 of Table 2.1. The effect of doubling or halving the electron percentage in the beam on the pion relative content is displayed in red in Figure 2.4. We reserve a slightly different treatment for the muon content. Since G4Beamline tracks only particles which cross all the wire chambers, pion events that decay in flight from WC1 to WC4 are not recorded by G4Beamline. Pion decays in the beamline could be trigger the beamline detectors in data, if the produced muon proceeds in the beamline. Thus, we take the G4Beamline prediction for muons as a lower bound in the composition: the effect of doubling the muon content (line 2 in Table 2.1) is shown in blue on Figure 2.4. A future study of data from additional beamline detectors such as the Aerogel Chernkov detectors [42] or the muon range stack (see Section ??) has the potential of a narrowing the systematics uncertainty coming from the beamline composition.

We propagate the uncertainty on the beamline composition as a systematic uncertainty to the cross section by varying the beam composition for all the cases listed in Table 2.1 and evaluating variation of obtained data cross sections in each bin. This systematic uncertainty is summed in quadrature with the statistical uncertainty and the systematic uncertainty related to the kinetic energy measurement.

	Magnet Current -60A			Magnet Current -100 A		
	MC π^-	MC μ^-	MC e^-	MC π^-	MC μ^-	MC e^-
Expected Composition	68.8 %	4.6 %	26.6 %	87.4 %	3.7 %	8.9 %
Composition 2x Muons	64.2 %	9.2 %	26.6 %	83.7 %	7.4 %	8.9 %
Composition 2x Electrons	42.2 %	4.6 %	53.2 %	78.5 %	3.7 %	17.8 %
Composition 0.5x Electrons	82.1 %	4.6 %	13.3 %	91.9 %	3.7 %	4.4 %

Table 2.1: Beam composition variation for the study of systematics due to beam contamination.

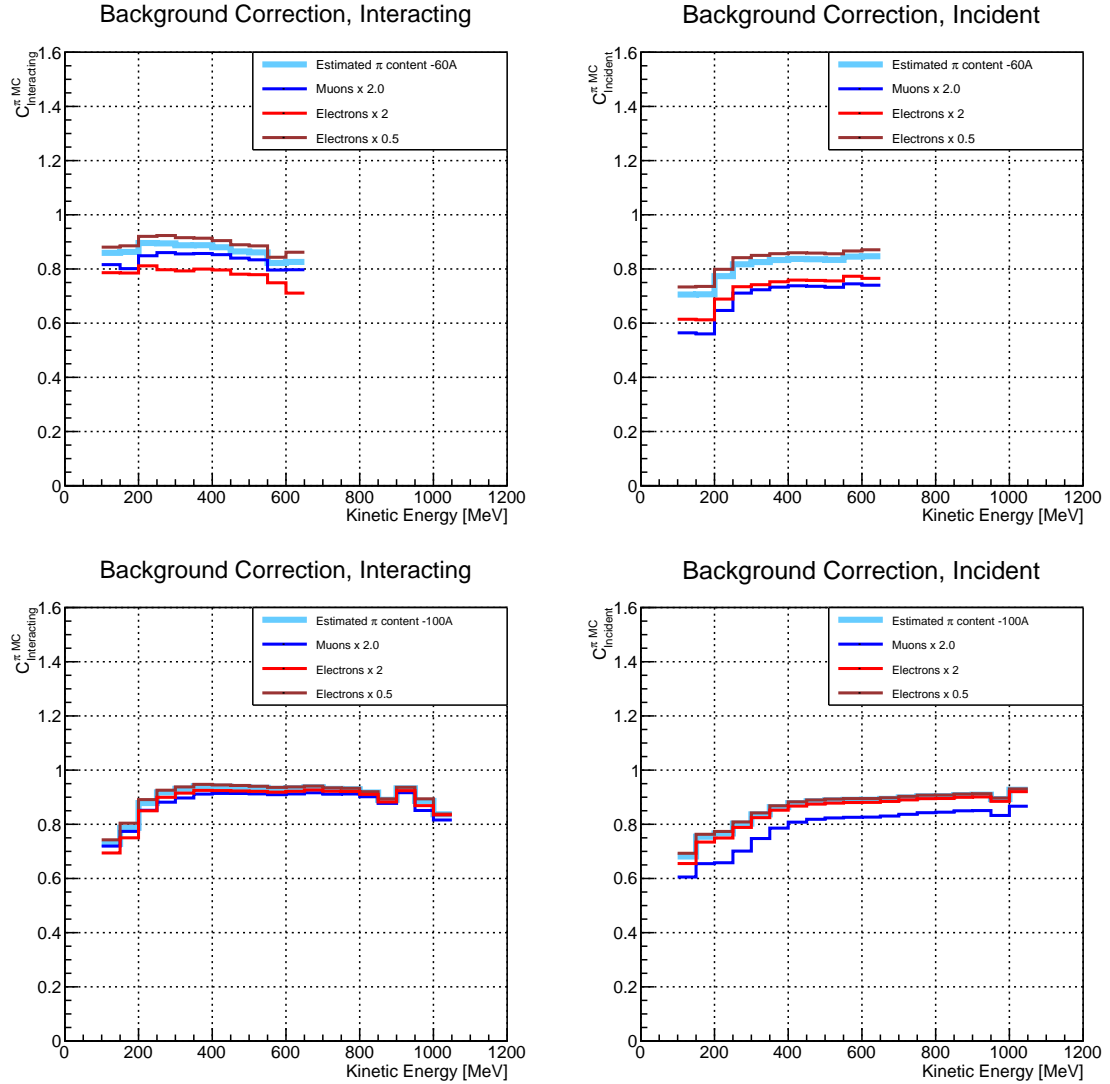


Figure 2.4: *Left:* MC estimated relative pion content for interacting histogram a function of kinetic energy for the 60A runs (top) and 100A runs (bottom), statistics uncertainty in azure and systematic uncertainty in blue. *Right:* MC estimated relative pion content for incident histogram a function of kinetic energy for the 60A runs (top) and 100A (bottom), statistics uncertainty in azure and systematic uncertainty in blue.

2.2.2 Efficiency Correction

The interaction point for a track used in the total hadronic cross section analysis is defined to be the last point of the WC2TPC matched track which lies inside the fiducial volume. This definition is independent from the topology of the interaction. If the TPC track stops within the fiducial volume, its last point will be the interaction point, no matter what the products of the interaction look like; if the track crosses the boundaries of the fiducial volume, the track will be considered “through going” and no interaction point will be found. Given this definition, it is evident that we rely on the tracking algorithm to discern where the interaction occurred in the TPC and correctly stop the tracking. The tracking algorithm has an intrinsic angle resolution as shown in section 1.5.3, which limits its efficiency, especially in the case of elastic scattering occurring at low angles. Thus, we need to apply an efficiency correction to data in order to retrieve the true cross section. The efficiency correction is evaluated separately for the interacting and incident histograms, namely ϵ_i^{int} and ϵ_i^{inc} , and propagated to the cross section as shown in equation 8.

Efficiency Correction: Procedure

We describe here the procedure to calculate the efficiency correction taking the interacting histogram as example and noting that the procedure is identical for the incident histogram.

We derive the correction on a set of pure pion MC, calculating its value bin by bin as the ratio between the true bin content and the correspondent reconstructed bin content. The correction is then applied to the relevant bin in data. In formulae, the efficiency correction is calculated to be

$$\epsilon_i^{int} = \frac{N_{\text{Interacting}}^{\pi \text{ Reco MC}}(E_i)}{N_{\text{Interacting}}^{\pi \text{ True MC}}(E_i)}, \quad (2.9)$$

904 where $N_{\text{Interacting}}^{\pi \text{ True MC}}(E_i)$ is the content of the i -th bin in for the true interacting
 905 histogram, and $N_{\text{Interacting}}^{\pi \text{ Reco MC}}(E_i)$ is the content of the i -th bin in for the reconstructed
 906 interacting histogram. The correction is applied to data as follows

$$N_{\text{Interacting}}^{\pi \text{ True Data}}(E_i) = \frac{N_{\text{Interacting}}^{\pi \text{ Reco Data}}(E_i)}{\epsilon_i^{\text{int}}} = N_{\text{Interacting}}^{\pi \text{ Reco Data}}(E_i) \frac{N_{\text{Interacting}}^{\pi \text{ True MC}}(E_i)}{N_{\text{Interacting}}^{\pi \text{ Reco MC}}(E_i)}. \quad (2.10)$$

907 where $N_{\text{Interacting}}^{\pi \text{ Reco Data}}(E_i)$ is the background subtracted bin content of the i -th bin in
 908 for the reconstructed interacting histogram for data, i.e.

$$N_{\text{Interacting}}^{\pi \text{ Reco Data}}(E_i) = N_{\text{Interacting}}^{\text{TOT Data}}(E_i) - B_{\text{Interacting}}^{\text{Data}}(E_i) = C_{\text{Interacting}}^{\pi \text{ MC}}(E_i) N_{\text{Interacting}}^{\text{TOT Data}}(E_i). \quad (2.11)$$

909 Figures ?? show $\epsilon_i^{\text{int}}(E_i)$ and $\epsilon_i^{\text{int}}(E_i)$ as a function of the kinetic energy for the
 910 60A runs and their systematic uncertainty.

911 In section 1.5.3, we estimated the angular resolution for data and MC to be
 912 $\bar{\alpha}_{\text{Data}} = (5.0 \pm 4.5)$ deg and $\bar{\alpha}_{\text{MC}} = (4.5 \pm 3.9)$ deg, respectively. Interaction angles
 913 smaller than the angular resolution are indistinguishable for the reconstruction. Thus,
 914 we claim we are able to measure the cross section for interaction angles greater than
 915 5.0 deg. Geant4 simulates interactions at all angles, as shown in figure ?. In order
 916 to calculate the efficiency correction, we select events which have an interaction angle
 917 greater than a given α_{res} to construct the true interacting and incident histograms
 918 (the denominator of the efficiency correction).

919 The systematics on the efficiency correction is estimated by varying the value of
 920 α_{res} to be

921 Treatment of Systematics

2.3 Results

Figure 2.5 show the measurement of the (π^- -Ar) total hadronic cross section for scattering angles greater than 5° , as the result of the background subtraction and efficiency correction to the raw cross section. The top left plot is the measurement obtained on the 60A data, statistical uncertainty in black and systematic uncertainty in red. The top right plot is the measurement obtained on the 100A data, statistical uncertainty in black and systematic uncertainty in blue. The bottom plot shows the two measurements overlaid. In all three plot, the Geant4 prediction for the total hadronic cross section for angle scattering greater than 5° is displayed in green.

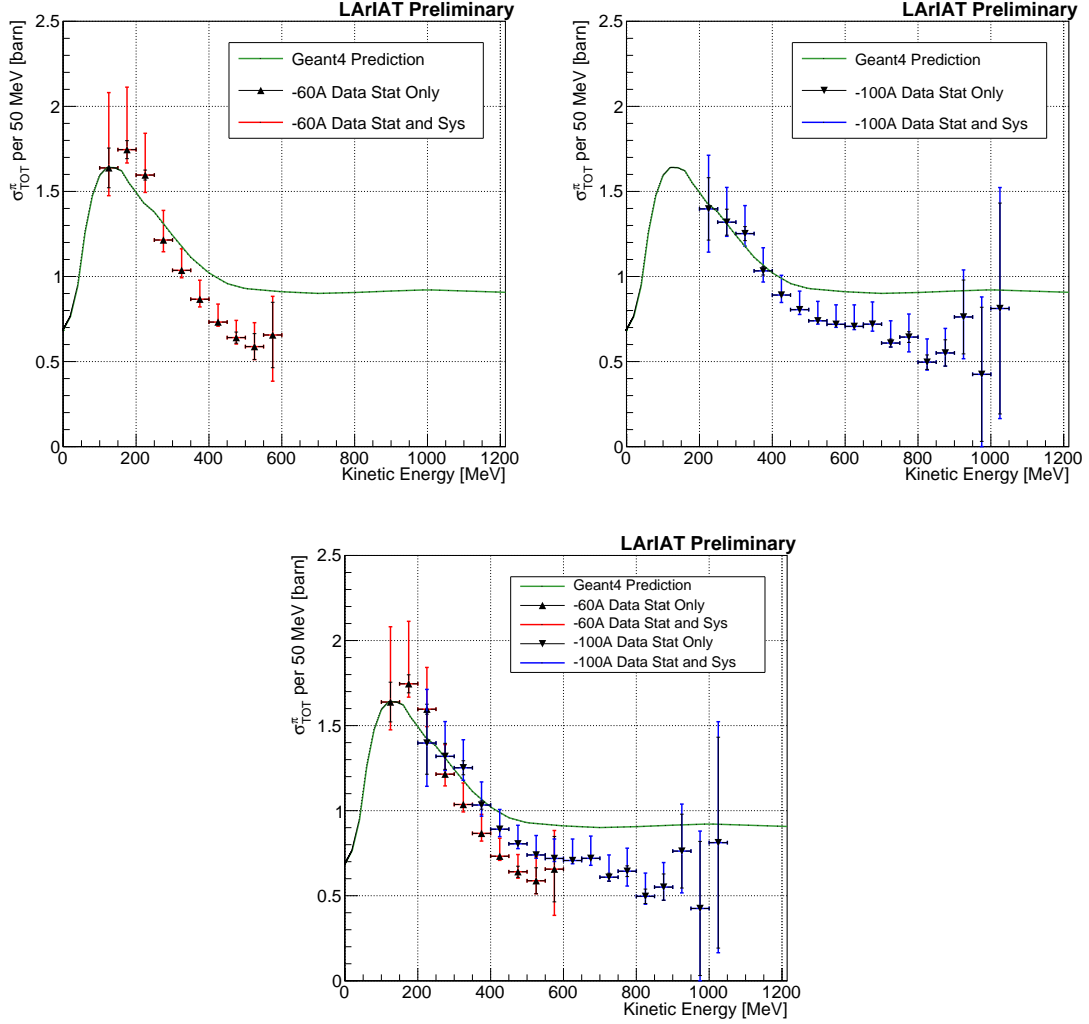


Figure 2.5: *Top Left:* (π^- -Ar) total hadronic cross section for scattering angles greater than 5° measured in the 60A sample, statistical uncertainty in black and systematic uncertainty in red. The Geant4 prediction for the total hadronic cross section for angle scattering greater than 5° is displayed in green.

Top Right: (π^- -Ar) total hadronic cross section for scattering angles greater than 5° measured in the 100A sample, statistical uncertainty in black and systematic uncertainty in blue. The Geant4 prediction for the total hadronic cross section for angle scattering greater than 5° is displayed in green.

Bottom: (π^- -Ar) total hadronic cross section measurements in the 60A and 100A samples overlaid with the Geant4 prediction (green).

931 **Appendix A**

932 **Kaon Analysis**

933 **A.1 Data Sample**

934 **A.2 Beamline Contamination**

935 **A.3 WC2TPC match**

936 **A.4 Cross Section**

937 **A.5 Future developments**

Bibliography

- [1] PDG Tables for Liquid Argon. . Technical report.
- [2] Precision electroweak measurements on the z resonance. *Physics Reports*, 427(5):257 – 454, 2006.
- [3] K. Abe, J. Amey, C. Andreopoulos, M. Antonova, S. Aoki, A. Ariga, D. Autiero, S. Ban, M. Barbi, G. J. Barker, G. Barr, C. Barry, P. Bartet-Friburg, M. Batkiewicz, V. Berardi, S. Berkman, S. Bhadra, S. Bienstock, A. Blondel, S. Bolognesi, S. Bordoni, S. B. Boyd, D. Brailsford, A. Bravar, C. Bronner, M. Buizza Avanzini, R. G. Calland, T. Campbell, S. Cao, S. L. Cartwright, M. G. Catanesi, A. Cervera, C. Checchia, D. Cherdack, N. Chikuma, G. Christodoulou, A. Clifton, J. Coleman, G. Collazuol, D. Coploue, A. Cudd, A. Dabrowska, G. De Rosa, T. Dealtry, P. F. Denner, S. R. Dennis, C. Densham, D. Dewhurst, F. Di Lodovico, S. Di Luise, S. Dolan, O. Drapier, K. E. Duffy, J. Dumarchez, M. Dziewiecki, S. Emery-Schrenk, A. Ereditato, T. Feusels, A. J. Finch, G. A. Fiorentini, M. Friend, Y. Fujii, D. Fukuda, Y. Fukuda, V. Galymov, A. Garcia, C. Giganti, F. Gizzarelli, T. Golan, M. Gonin, D. R. Hadley, L. Haegel, M. D. Haigh, D. Hansen, J. Harada, M. Hartz, T. Hasegawa, N. C. Hastings, T. Hayashino, Y. Hayato, R. L. Helmer, A. Hillairet, T. Hiraki, A. Hiramoto, S. Hirota, M. Hogan, J. Holeczek, F. Hosomi, K. Huang, A. K. Ichikawa, M. Ikeda, J. Imber, J. Insler, R. A. Intonti, T. Ishida, T. Ishii, E. Iwai, K. Iwamoto, A. Izmaylov, B. Jamieson, M. Jiang, S. Johnson, P. Jonsson,

959 C. K. Jung, M. Kabirnezhad, A. C. Kaboth, T. Kajita, H. Kakuno, J. Kameda,
 960 D. Karlen, T. Katori, E. Kearns, M. Khabibullin, A. Khotjantsev, H. Kim,
 961 J. Kim, S. King, J. Kisiel, A. Knight, A. Knox, T. Kobayashi, L. Koch, T. Koga,
 962 A. Konaka, K. Kondo, L. L. Kormos, A. Korzenev, Y. Koshio, K. Kowalik,
 963 W. Kropp, Y. Kudenko, R. Kurjata, T. Kutter, J. Lagoda, I. Lamont, M. Lam-
 964 oureux, E. Larkin, P. Lasorak, M. Laveder, M. Lawe, M. Licciardi, T. Lindner,
 965 Z. J. Liptak, R. P. Litchfield, X. Li, A. Longhin, J. P. Lopez, T. Lou, L. Ludovici,
 966 X. Lu, L. Magaletti, K. Mahn, M. Malek, S. Manly, A. D. Marino, J. F. Martin,
 967 P. Martins, S. Martynenko, T. Maruyama, V. Matveev, K. Mavrokoridis, W. Y.
 968 Ma, E. Mazzucato, M. McCarthy, N. McCauley, K. S. McFarland, C. McGrew,
 969 A. Mefodiev, C. Metelko, M. Mezzetto, P. Mijakowski, A. Minamino, O. Mi-
 970 neev, S. Mine, A. Missert, M. Miura, S. Moriyama, Th. A. Mueller, J. Myslik,
 971 T. Nakadaira, M. Nakahata, K. G. Nakamura, K. Nakamura, K. D. Nakamura,
 972 Y. Nakanishi, S. Nakayama, T. Nakaya, K. Nakayoshi, C. Nantais, C. Nielsen,
 973 M. Nirkko, K. Nishikawa, Y. Nishimura, P. Novella, J. Nowak, H. M. O’Keeffe,
 974 K. Okumura, T. Okusawa, W. Oryszczak, S. M. Oser, T. Ovsyannikova, R. A.
 975 Owen, Y. Oyama, V. Palladino, J. L. Palomino, V. Paolone, N. D. Patel,
 976 P. Paudyal, M. Pavin, D. Payne, J. D. Perkin, Y. Petrov, L. Pickard, L. Pick-
 977 ering, E. S. Pinzon Guerra, C. Pistillo, B. Popov, M. Posiadala-Zezula, J.-M.
 978 Poutissou, R. Poutissou, P. Przewlocki, B. Quilain, T. Radermacher, E. Radi-
 979 cioni, P. N. Ratoff, M. Ravonel, M. A. Rayner, A. Redij, E. Reinherz-Aronis,
 980 C. Riccio, P. A. Rodrigues, E. Rondio, B. Rossi, S. Roth, A. Rubbia, A. Rychter,
 981 K. Sakashita, F. Sánchez, E. Scantamburlo, K. Scholberg, J. Schwehr, M. Scott,
 982 Y. Seiya, T. Sekiguchi, H. Sekiya, D. Sgalaberna, R. Shah, A. Shaikhiev,
 983 F. Shaker, D. Shaw, M. Shiozawa, T. Shirahige, S. Short, M. Smy, J. T.
 984 Sobczyk, H. Sobel, M. Sorel, L. Southwell, J. Steinmann, T. Stewart, P. Stowell,
 985 Y. Suda, S. Suvorov, A. Suzuki, S. Y. Suzuki, Y. Suzuki, R. Tacik, M. Tada,

986 A. Takeda, Y. Takeuchi, H. K. Tanaka, H. A. Tanaka, D. Terhorst, R. Terri,
 987 T. Thakore, L. F. Thompson, S. Tobayama, W. Toki, T. Tomura, C. Tourama-
 988 nis, T. Tsukamoto, M. Tzanov, Y. Uchida, M. Vagins, Z. Vallari, G. Vasseur,
 989 T. Vladisavljevic, T. Wachala, C. W. Walter, D. Wark, M. O. Wascko, A. We-
 990 ber, R. Wendell, R. J. Wilkes, M. J. Wilking, C. Wilkinson, J. R. Wilson, R. J.
 991 Wilson, C. Wret, Y. Yamada, K. Yamamoto, M. Yamamoto, C. Yanagisawa,
 992 T. Yano, S. Yen, N. Yershov, M. Yokoyama, K. Yoshida, T. Yuan, M. Yu, A. Za-
 993 lewska, J. Zalipska, L. Zambelli, K. Zaremba, M. Ziembicki, E. D. Zimmerman,
 994 M. Zito, and J. Żmuda. Combined analysis of neutrino and antineutrino oscil-
 995 lations at t2k. *Phys. Rev. Lett.*, 118:151801, Apr 2017.

996 [4] K. Abe, Y. Haga, Y. Hayato, M. Ikeda, K. Iyogi, J. Kameda, Y. Kishimoto,
 997 M. Miura, S. Moriyama, M. Nakahata, T. Nakajima, Y. Nakano, S. Nakayama,
 998 A. Orii, H. Sekiya, M. Shiozawa, A. Takeda, H. Tanaka, T. Tomura, R. A. Wen-
 999 dell, R. Akutsu, T. Irvine, T. Kajita, K. Kaneyuki, Y. Nishimura, E. Richard,
 1000 K. Okumura, L. Labarga, P. Fernandez, J. Gustafson, C. Kachulis, E. Kearns,
 1001 J. L. Raaf, J. L. Stone, L. R. Sulak, S. Berkman, C. M. Nantais, H. A.
 1002 Tanaka, S. Tobayama, M. Goldhaber, W. R. Kropp, S. Mine, P. Weatherly,
 1003 M. B. Smy, H. W. Sobel, V. Takhistov, K. S. Ganezer, B. L. Hartfiel, J. Hill,
 1004 N. Hong, J. Y. Kim, I. T. Lim, R. G. Park, A. Himmel, Z. Li, E. O’Sullivan,
 1005 K. Scholberg, C. W. Walter, T. Wongjirad, T. Ishizuka, S. Tasaka, J. S. Jang,
 1006 J. G. Learned, S. Matsuno, S. N. Smith, M. Friend, T. Hasegawa, T. Ishida,
 1007 T. Ishii, T. Kobayashi, T. Nakadaira, K. Nakamura, Y. Oyama, K. Sakashita,
 1008 T. Sekiguchi, T. Tsukamoto, A. T. Suzuki, Y. Takeuchi, T. Yano, S. V. Cao,
 1009 T. Hiraki, S. Hirota, K. Huang, T. Kikawa, A. Minamino, T. Nakaya, K. Suzuki,
 1010 Y. Fukuda, K. Choi, Y. Itow, T. Suzuki, P. Mijakowski, K. Frankiewicz, J. Hig-
 1011 night, J. Imber, C. K. Jung, X. Li, J. L. Palomino, M. J. Wilking, C. Yanag-
 1012 isawa, D. Fukuda, H. Ishino, T. Kayano, A. Kibayashi, Y. Koshio, T. Mori,

1013 M. Sakuda, C. Xu, Y. Kuno, R. Tacik, S. B. Kim, H. Okazawa, Y. Choi,
1014 K. Nishijima, M. Koshihara, Y. Totsuka, Y. Suda, M. Yokoyama, C. Bronner,
1015 M. Hartz, K. Martens, Ll. Marti, Y. Suzuki, M. R. Vagins, J. F. Martin, A. Kon-
1016 aka, S. Chen, Y. Zhang, and R. J. Wilkes. Search for proton decay via $p \rightarrow e^+ \pi^0$
1017 and $p \rightarrow \mu^+ \pi^0$ in 0.31 megaton \cdot years exposure of the super-kamiokande water
1018 cherenkov detector. *Phys. Rev. D*, 95:012004, Jan 2017.

1019 [5] R Acciarri, C Adams, J Asaadi, B Baller, T Bolton, C Bromberg, F Ca-
1020 vanna, E Church, D Edmunds, A Ereditato, S Farooq, B Fleming, H Greenlee,
1021 G Horton-Smith, C James, E Klein, K Lang, P Laurens, D McKee, R Mehdiyev,
1022 B Page, O Palamara, K Partyka, G Rameika, B Rebel, M Soderberg, J Spitz,
1023 A M Szelc, M Weber, M Wojcik, T Yang, and G P Zeller. A study of electron
1024 recombination using highly ionizing particles in the argoneut liquid argon tpc.
1025 *Journal of Instrumentation*, 8(08):P08005, 2013.

1026 [6] R Acciarri, M Antonello, B Baibussinov, M Baldo-Ceolin, P Benetti,
1027 F Calaprice, E Calligarich, M Cambiaghi, N Canci, F Carbonara, F Cavanna,
1028 S Centro, A G Cocco, F Di Pompeo, G Fiorillo, C Galbiati, V Gallo, L Grandi,
1029 G Meng, I Modena, C Montanari, O Palamara, L Pandola, G B Piano Mortari,
1030 F Pietropaolo, G L Raselli, M Roncadelli, M Rossella, C Rubbia, E Segreto,
1031 A M Szelc, S Ventura, and C Vignoli. Effects of nitrogen contamination in
1032 liquid argon. *Journal of Instrumentation*, 5(06):P06003, 2010.

1033 [7] R. Acciarri et al. Demonstration and Comparison of Operation of Photomulti-
1034 plier Tubes at Liquid Argon Temperature. *JINST*, 7:P01016, 2012.

1035 [8] R. Acciarri et al. Design and Construction of the MicroBooNE Detector. *JINST*,
1036 12(02):P02017, 2017.

- [9] R. Acciarri et al. First Observation of Low Energy Electron Neutrinos in a Liquid Argon Time Projection Chamber. *Phys. Rev.*, D95(7):072005, 2017. [Phys. Rev.D95,072005(2017)].
- [10] M Adamowski, B Carls, E Dvorak, A Hahn, W Jaskierny, C Johnson, H Jostlein, C Kendziora, S Lockwitz, B Pahlka, R Plunkett, S Pordes, B Rebel, R Schmitt, M Stancari, T Tope, E Voirin, and T Yang. The liquid argon purity demonstrator. *Journal of Instrumentation*, 9(07):P07005, 2014.
- [11] C. Adams et al. The Long-Baseline Neutrino Experiment: Exploring Fundamental Symmetries of the Universe. 2013.
- [12] P. Adamson, L. Aliaga, D. Ambrose, N. Anfimov, A. Antoshkin, E. Arrieta-Diaz, K. Augsten, A. Aurisano, C. Backhouse, M. Baird, B. A. Bambah, K. Bays, B. Behera, S. Bending, R. Bernstein, V. Bhatnagar, B. Bhuyan, J. Bian, T. Blackburn, A. Bolshakova, C. Bromberg, J. Brown, G. Brunetti, N. Buchanan, A. Butkevich, V. Bychkov, M. Campbell, E. Catano-Mur, S. Childress, B. C. Choudhary, B. Chowdhury, T. E. Coan, J. A. B. Coelho, M. Colo, J. Cooper, L. Corwin, L. Cremonesi, D. Cronin-Hennessy, G. S. Davies, J. P. Davies, P. F. Derwent, R. Dharmapalan, P. Ding, Z. Djurcic, E. C. Dukes, H. Duyang, S. Edayath, R. Ehrlich, G. J. Feldman, M. J. Frank, M. Gabrielyan, H. R. Gallagher, S. Germani, T. Ghosh, A. Giri, R. A. Gomes, M. C. Goodman, V. Grichine, R. Group, D. Grover, B. Guo, A. Habig, J. Hartnell, R. Hatcher, A. Hatzikoutelis, K. Heller, A. Himmel, A. Holin, J. Hylen, F. Jediny, M. Judah, G. K. Kafka, D. Kalra, S. M. S. Kasahara, S. Kasetti, R. Keloth, L. Kolupaeva, S. Kotelnikov, I. Kourbanis, A. Kreymer, A. Kumar, S. Kurbanov, K. Lang, W. M. Lee, S. Lin, J. Liu, M. Lokajicek, J. Lozier, S. Luchuk, K. Maan, S. Magill, W. A. Mann, M. L. Marshak, K. Matera, V. Matveev, D. P. Méndez, M. D. Messier, H. Meyer, T. Miao, W. H. Miller, S. R. Mishra, R. Mohanta, A. Moren,

1063 L. Mualem, M. Muether, S. Mufson, R. Murphy, J. Musser, J. K. Nelson,
1064 R. Nichol, E. Niner, A. Norman, T. Nosek, Y. Oksuzian, A. Olshevskiy, T. Ol-
1065 son, J. Paley, P. Pandey, R. B. Patterson, G. Pawloski, D. Pershey, O. Petrova,
1066 R. Petti, S. Phan-Budd, R. K. Plunkett, R. Poling, B. Potukuchi, C. Principato,
1067 F. Psihas, A. Radovic, R. A. Rameika, B. Rebel, B. Reed, D. Rocco, P. Rojas,
1068 V. Ryabov, K. Sachdev, P. Sail, O. Samoylov, M. C. Sanchez, R. Schroeter,
1069 J. Sepulveda-Quiroz, P. Shanahan, A. Sheshukov, J. Singh, J. Singh, P. Singh,
1070 V. Singh, J. Smolik, N. Solomey, E. Song, A. Sousa, K. Soustruznik, M. Strait,
1071 L. Suter, R. L. Talaga, M. C. Tamsett, P. Tas, R. B. Thayyullathil, J. Thomas,
1072 X. Tian, S. C. Tognini, J. Tripathi, A. Tsaris, J. Urheim, P. Vahle, J. Vasel,
1073 L. Vinton, A. Vold, T. Vrba, B. Wang, M. Wetstein, D. Whittington, S. G. Wo-
1074 jcicki, J. Wolcott, N. Yadav, S. Yang, J. Zalesak, B. Zamorano, and R. Zwaska.
1075 Constraints on oscillation parameters from ν_e appearance and ν_μ disappearance
1076 in nova. *Phys. Rev. Lett.*, 118:231801, Jun 2017.

1077 [13] Alan Agresti. *Categorical Data Analysis*. Wiley Series in Probability and Statis-
1078 tics. Wiley, 2013.

1079 [14] A. Aguilar-Arevalo et al. Evidence for neutrino oscillations from the observation
1080 of anti-neutrino(electron) appearance in a anti-neutrino(muon) beam. *Phys.*
1081 *Rev.*, D64:112007, 2001.

1082 [15] A. A. Aguilar-Arevalo et al. Improved Search for $\bar{\nu}_\mu \rightarrow \bar{\nu}_e$ Oscillations in the
1083 MiniBooNE Experiment. *Phys. Rev. Lett.*, 110:161801, 2013.

1084 [16] S. Amoruso et al. Study of electron recombination in liquid argon with the
1085 ICARUS TPC. *Nucl. Instrum. Meth.*, A523:275–286, 2004.

1086 [17] C. Anderson et al. The ArgoNeuT Detector in the NuMI Low-Energy beam
1087 line at Fermilab. *JINST*, 7:P10019, 2012.

- 1088 [18] C. Andreopoulos et al. The GENIE Neutrino Monte Carlo Generator. *Nucl.*
1089 *Instrum. Meth.*, A614:87–104, 2010.
- 1090 [19] Timofei Bolshakov Andrey Petrov. Java synoptic toolkit. Technical report,
1091 Sept 2010.
- 1092 [20] M. Antonello, B. Baibussinov, P. Benetti, E. Calligarich, N. Canci, S. Cen-
1093 tro, A. Cesana, K. Cieslik, D. B. Cline, A. G. Cocco, A. Dabrowska, D. De-
1094 qual, A. Dermenev, R. Dolfini, C. Farnese, A. Fava, A. Ferrari, G. Fiorillo,
1095 D. Gibin, S. Gninenko, A. Guglielmi, M. Haranczyk, J. Holeczek, A. Ivashkin,
1096 J. Kisiel, I. Kochanek, J. Lagoda, S. Mania, A. Menegolli, G. Meng, C. Monta-
1097 nari, S. Otwinowski, A. Piazzoli, P. Picchi, F. Pietropaolo, P. Plonski, A. Rap-
1098 poldi, G. L. Raselli, M. Rossella, C. Rubbia, P. Sala, A. Scaramelli, E. Seg-
1099 reto, F. Sergiampietri, D. Stefan, J. Stepaniak, R. Sulej, M. Szarska, M. Ter-
1100 rani, F. Varanini, S. Ventura, C. Vignoli, H. Wang, X. Yang, A. Zalewska,
1101 and K. Zaremba. Precise 3d track reconstruction algorithm for the ICARUS
1102 t600 liquid argon time projection chamber detector. *Advances in High Energy*
1103 *Physics*, 2013:1–16, 2013.
- 1104 [21] M. Antonello et al. A Proposal for a Three Detector Short-Baseline Neutrino
1105 Oscillation Program in the Fermilab Booster Neutrino Beam. 2015.
- 1106 [22] D. Ashery, I. Navon, G. Azuelos, H. K. Walter, H. J. Pfeiffer, and F. W.
1107 Schlepütz. True absorption and scattering of pions on nuclei. *Phys. Rev. C*,
1108 23:2173–2185, May 1981.
- 1109 [23] C. Athanassopoulos et al. Evidence for $\nu(\mu) \rightarrow \nu(e)$ neutrino oscillations
1110 from LSND. *Phys. Rev. Lett.*, 81:1774–1777, 1998.

- 1111 [24] Borut Bajc, Junji Hisano, Takumi Kuwahara, and Yuji Omura. Threshold
1112 corrections to dimension-six proton decay operators in non-minimal {SUSY}
1113 su(5) {GUTs}. *Nuclear Physics B*, 910:1 – 22, 2016.
- 1114 [25] B. Baller. Trajcluster user guide. Technical report, apr 2016.
- 1115 [26] Gary Barker. Neutrino event reconstruction in a liquid argon TPC. *Journal of*
1116 *Physics: Conference Series*, 308:012015, jul 2011.
- 1117 [27] BASF Corp. 100 Park Avenue, Florham Park, NJ 07932 USA.
- 1118 [28] R. Becker-Szendy, C. B. Bratton, D. R. Cady, D. Casper, R. Claus, M. Crouch,
1119 S. T. Dye, W. Gajewski, M. Goldhaber, T. J. Haines, P. G. Halverson, T. W.
1120 Jones, D. Kielczewska, W. R. Kropp, J. G. Learned, J. M. LoSecco, C. Mc-
1121 Grew, S. Matsuno, J. Matthews, M. S. Mudah, L. Price, F. Reines, J. Schultz,
1122 D. Sinclair, H. W. Sobel, J. L. Stone, L. R. Sulak, R. Svoboda, G. Thornton,
1123 and J. C. van der Velde. Search for proton decay into $e^+ + \pi^0$ in the imb-3
1124 detector. *Phys. Rev. D*, 42:2974–2976, Nov 1990.
- 1125 [29] J B Birks. Scintillations from organic crystals: Specific fluorescence and relative
1126 response to different radiations. *Proceedings of the Physical Society. Section A*,
1127 64(10):874, 1951.
- 1128 [30] A. Bodek and J. L. Ritchie. Further studies of fermi-motion effects in lepton
1129 scattering from nuclear targets. *Phys. Rev. D*, 24:1400–1402, Sep 1981.
- 1130 [31] Mark G. Boulay and A. Hime. Direct WIMP detection using scintillation time
1131 discrimination in liquid argon. 2004.
- 1132 [32] D. V. Bugg, R. S. Gilmore, K. M. Knight, D. C. Salter, G. H. Stafford, E. J. N.
1133 Wilson, J. D. Davies, J. D. Dowell, P. M. Hattersley, R. J. Homer, A. W. O’dell,

1134 A. A. Carter, R. J. Tapper, and K. F. Riley. Kaon-nucleon total cross sections
1135 from 0.6 to 2.65 gev/ *c. Phys. Rev.*, 168:1466–1475, Apr 1968.

1136 [33] W. M. Burton and B. A. Powell. Fluorescence of tetraphenyl-butadiene in the
1137 vacuum ultraviolet. *Applied Optics*, 12(1):87, jan 1973.

1138 [34] CAEN. Caen v1495 data sheet. Technical report, jan 2018.

1139 [35] CAEN. Caen v1740 data sheet. Technical report, jan 2018.

1140 [36] A. S. Carroll, I. H. Chiang, C. B. Dover, T. F. Kycia, K. K. Li, P. O. Mazur,
1141 D. N. Michael, P. M. Mockett, D. C. Rahm, and R. Rubinstein. Pion-nucleus
1142 total cross sections in the (3,3) resonance region. *Phys. Rev. C*, 14:635–638,
1143 Aug 1976.

1144 [37] D. Casper. The nuance neutrino physics simulation, and the future. *Nuclear*
1145 *Physics B - Proceedings Supplements*, 112(1-3):161–170, nov 2002.

1146 [38] A. Cervera, A. Donini, M.B. Gavela, J.J. Gomez Cadenas, P. Hernandez,
1147 O. Mena, and S. Rigolin. Golden measurements at a neutrino factory. *Nu-*
1148 *clear Physics B*, 579(1-2):17–55, jul 2000.

1149 [39] E. Church. LArSoft: A Software Package for Liquid Argon Time Projection
1150 Drift Chambers. 2013.

1151 [40] ATLAS Collaboration. Observation of a new particle in the search for the
1152 standard model higgs boson with the ATLAS detector at the LHC. *Physics*
1153 *Letters B*, 716(1):1–29, sep 2012.

1154 [41] CMS Collaboration. Observation of a new boson at a mass of 125 gev with the
1155 cms experiment at the lh. *Physics Letters B*, 716(1):30 – 61, 2012.

1156 [42] The LArIAT Collaboration. The liquid argon in a testbeam (lariat) experiment.
1157 Technical report, In Preparation 2018.

- 1158 [43] Stefano Dell’Oro, Simone Marcocci, Matteo Viel, and Francesco Vissani. Neu-
1159 trinoless double beta decay: 2015 review. *Advances in High Energy Physics*,
1160 2016:1–37, 2016.
- 1161 [44] S.E. Derenzo, A.R. Kirschbaum, P.H. Eberhard, R.R. Ross, and F.T. Solmitz.
1162 Test of a liquid argon chamber with 20 m rms resolution. *Nuclear Instruments*
1163 *and Methods*, 122:319 – 327, 1974.
- 1164 [45] Savas Dimopoulos, Stuart Raby, and Frank Wilczek. Proton Decay in Super-
1165 symmetric Models. *Phys. Lett.*, B112:133, 1982.
- 1166 [46] D. Drakoulakos et al. Proposal to perform a high-statistics neutrino scattering
1167 experiment using a fine-grained detector in the NuMI beam. 2004.
- 1168 [47] A Ereditato, C C Hsu, S Janos, I Kreslo, M Messina, C Rudolf von Rohr,
1169 B Rossi, T Strauss, M S Weber, and M Zeller. Design and operation of
1170 argontube: a 5 m long drift liquid argon tpc. *Journal of Instrumentation*,
1171 8(07):P07002, 2013.
- 1172 [48] Torleif Ericson and Wolfram Weise. *Pions and Nuclei (The International Series*
1173 *of Monographs on Physics)*. Oxford University Press, 1988.
- 1174 [49] A.A. Aguilar-Arevalo et al. The miniboone detector. *Nuclear Instruments and*
1175 *Methods in Physics Research Section A: Accelerators, Spectrometers, Detectors*
1176 *and Associated Equipment*, 599(1):28 – 46, 2009.
- 1177 [50] Antonio Bueno et al. Nucleon decay searches with large liquid argon TPC de-
1178 tectors at shallow depths: atmospheric neutrinos and cosmogenic backgrounds.
1179 *Journal of High Energy Physics*, 2007(04):041–041, apr 2007.
- 1180 [51] A.S. Clough et al. Pion-nucleus total cross sections from 88 to 860 MeV. *Nuclear*
1181 *Physics B*, 76(1):15–28, jul 1974.

- 1182 [52] B.W. Allardyce et al. Pion reaction cross sections and nuclear sizes. *Nuclear*
1183 *Physics A*, 209(1):1 – 51, 1973.
- 1184 [53] C Athanassopoulos et al. The liquid scintillator neutrino detector and LAMPF
1185 neutrino source. *Nuclear Instruments and Methods in Physics Research Section*
1186 *A: Accelerators, Spectrometers, Detectors and Associated Equipment*, 388(1-
1187 2):149–172, mar 1997.
- 1188 [54] F. Binon et al. Scattering of negative pions on carbon. *Nuclear Physics B*,
1189 17(1):168 – 188, 1970.
- 1190 [55] L. Aliaga et al. Minerva neutrino detector response measured with test beam
1191 data. *Nuclear Instruments and Methods in Physics Research Section A: Ac-*
1192 *celerators, Spectrometers, Detectors and Associated Equipment*, 789:28 – 42,
1193 2015.
- 1194 [56] M Adamowski et al. The liquid argon purity demonstrator. *Journal of Instru-*
1195 *mentation*, 9(07):P07005, 2014.
- 1196 [57] P. Vilain et al. Coherent single charged pion production by neutrinos. *Physics*
1197 *Letters B*, 313(1-2):267–275, aug 1993.
- 1198 [58] R. Acciarri et al. Convolutional neural networks applied to neutrino events
1199 in a liquid argon time projection chamber. *Journal of Instrumentation*,
1200 12(03):P03011, 2017.
- 1201 [59] R. Acciarri et al. Design and construction of the MicroBooNE detector. *Journal*
1202 *of Instrumentation*, 12(02):P02017–P02017, feb 2017.
- 1203 [60] C. E. Aalseth et al. DarkSide-20k: A 20 tonne two-phase LAr TPC for direct
1204 dark matter detection at LNGS. *The European Physical Journal Plus*, 133(3),
1205 mar 2018.

- [61] H Fenker. Standard beam pwc for fermilab. Technical report, Fermi National Accelerator Lab., Batavia, IL (USA), 1983.
- [62] H Fesbach. Theoretical nuclear physics: Nuclear reactions. 1992.
- [63] J. A. Formaggio and G. P. Zeller. From ev to eev: Neutrino cross sections across energy scales. *Rev. Mod. Phys.*, 84:1307–1341, Sep 2012.
- [64] E. Friedman et al. K+ nucleus reaction and total cross-sections: New analysis of transmission experiments. *Phys. Rev.*, C55:1304–1311, 1997.
- [65] V.M. Gehman, S.R. Seibert, K. Rielage, A. Hime, Y. Sun, D.-M. Mei, J. Maassen, and D. Moore. Fluorescence efficiency and visible re-emission spectrum of tetraphenyl butadiene films at extreme ultraviolet wavelengths. *Nuclear Instruments and Methods in Physics Research Section A: Accelerators, Spectrometers, Detectors and Associated Equipment*, 654(1):116 – 121, 2011.
- [66] H. Geiger and E. Marsden. On a diffuse reflection of the formula-particles. *Proceedings of the Royal Society A: Mathematical, Physical and Engineering Sciences*, 82(557):495–500, jul 1909.
- [67] Howard Georgi and S. L. Glashow. Unity of all elementary-particle forces. *Phys. Rev. Lett.*, 32:438–441, Feb 1974.
- [68] D.Y. Wong (editor) G.L. Shaw (Editor). *Pion-nucleon Scattering*. John Wiley & Sons Inc, 1969.
- [69] Glassman High Voltage, Inc., Precision Regulated High Voltage DC Power Supply.
- [70] D S Gorbunov. Sterile neutrinos and their role in particle physics and cosmology. *Physics-Uspekhi*, 57(5):503, 2014.

- 1229 [71] C. Green, J. Kowalkowski, M. Paterno, M. Fischler, L. Garren, and Q. Lu. The
1230 Art Framework. *J. Phys. Conf. Ser.*, 396:022020, 2012.
- 1231 [72] S. Hansen, D. Jensen, G. Savage, E. Skup, and A. Soha. Fermilab test beam
1232 multi-wire proportional chamber tracking system upgrade. June 2014. Interna-
1233 tional Conference on Technology and Instrumentation in Particle Physics (TIPP
1234 2014).
- 1235 [73] J. Harada. Non-maximal θ_{23} , large θ_{13} and tri-bimaximal θ_{12} via quark-
1236 lepton complementarity at next-to-leading order. *EPL (Europhysics Letters)*,
1237 103(2):21001, 2013.
- 1238 [74] Peter W. Higgs. Broken symmetries and the masses of gauge bosons. *Physical*
1239 *Review Letters*, 13(16):508–509, oct 1964.
- 1240 [75] P.W. Higgs. Broken symmetries, massless particles and gauge fields. *Physics*
1241 *Letters*, 12(2):132–133, sep 1964.
- 1242 [76] H J Hilke. Time projection chambers. *Reports on Progress in Physics*,
1243 73(11):116201, 2010.
- 1244 [77] N. Ishida, M. Chen, T. Doke, K. Hasuike, A. Hitachi, M. Gaudreau, M. Kase,
1245 Y. Kawada, J. Kikuchi, T. Komiyama, K. Kuwahara, K. Masuda, H. Okada,
1246 Y.H. Qu, M. Suzuki, and T. Takahashi. Attenuation length measurements of
1247 scintillation light in liquid rare gases and their mixtures using an improved
1248 reflection suppresser. *Nuclear Instruments and Methods in Physics Research*
1249 *Section A: Accelerators, Spectrometers, Detectors and Associated Equipment*,
1250 384(2-3):380–386, jan 1997.
- 1251 [78] G. Pulliam J. Asaadi, E. Gramellini. Determination of the electron lifetime in
1252 lariat. Technical report, August 2017.

- 1253 [79] George Jaffé. Zur theorie der ionisation in kolonnen. *Annalen der Physik*,
1254 347(12):303–344, 1913.
- 1255 [80] C. Jarlskog. A basis independent formulation of the connection between quark
1256 mass matrices, CP violation and experiment. *Zeitschrift für Physik C Particles
1257 and Fields*, 29(3):491–497, sep 1985.
- 1258 [81] B J P Jones, C S Chiu, J M Conrad, C M Ignarra, T Katori, and M Toups. A
1259 measurement of the absorption of liquid argon scintillation light by dissolved ni-
1260 trogen at the part-per-million level. *Journal of Instrumentation*, 8(07):P07011,
1261 2013.
- 1262 [82] Benjamin J. P. Jones. *Sterile Neutrinos in Cold Climates*. PhD thesis, MIT,
1263 2015.
- 1264 [83] Cezary Juszczak, Jarosław A. Nowak, and Jan T. Sobczyk. Simulations from
1265 a new neutrino event generator. *Nuclear Physics B - Proceedings Supplements*,
1266 159:211–216, sep 2006.
- 1267 [84] D. I. Kazakov. Beyond the standard model: In search of supersymmetry. In
1268 *2000 European School of high-energy physics, Caramulo, Portugal, 20 Aug-2
1269 Sep 2000: Proceedings*, pages 125–199, 2000.
- 1270 [85] Dae-Gyu Lee, R. N. Mohapatra, M. K. Parida, and Merostar Rani. Predic-
1271 tions for the proton lifetime in minimal nonsupersymmetric $so(10)$ models: An
1272 update. *Phys. Rev. D*, 51:229–235, Jan 1995.
- 1273 [86] M A Leigui de Oliveira. Expression of Interest for a Full-Scale Detector Engi-
1274 neering Test and Test Beam Calibration of a Single-Phase LAr TPC. Technical
1275 Report CERN-SPSC-2014-027. SPSC-EOI-011, CERN, Geneva, Oct 2014.

- [87] W. H. Lippincott, K. J. Coakley, D. Gastler, A. Hime, E. Kearns, D. N. McKinsey, J. A. Nikkel, and L. C. Stonehill. Scintillation time dependence and pulse shape discrimination in liquid argon. *Phys. Rev. C*, 78:035801, Sep 2008.
- [88] Jorge L. Lopez and Dimitri V. Nanopoulos. Flipped SU(5): Origins and recent developments. In *15th Johns Hopkins Workshop on Current Problems in Particle Theory: Particle Physics from Underground to Heaven Baltimore, Maryland, August 26-28, 1991*, pages 277–297, 1991.
- [89] Vincent Lucas and Stuart Raby. Nucleon decay in a realistic so(10) susy gut. *Phys. Rev. D*, 55:6986–7009, Jun 1997.
- [90] Ettore Majorana. Teoria simmetrica dell’elettrone e del positrone. *Il Nuovo Cimento*, 14(4):171–184, apr 1937.
- [91] Hisakazu Minakata and Alexei Yu. Smirnov. Neutrino mixing and quark-lepton complementarity. *Phys. Rev. D*, 70:073009, Oct 2004.
- [92] M. Mooney. The microboone experiment and the impact of space charge effects. 2015.
- [93] E. Morikawa, R. Reininger, P. Görtler, V. Saile, and P. Laporte. Argon, krypton, and xenon excimer luminescence: From the dilute gas to the condensed phase. *The Journal of Chemical Physics*, 91(3):1469–1477, aug 1989.
- [94] FM Newcomer, S Tedja, R Van Berg, J Van der Spiegel, and HH Williams. A fast, low power, amplifier-shaper-discriminator for high rate straw tracking systems. *IEEE Transactions on Nuclear Science*, 40(4):630–636, 1993.
- [95] Emmy Noether. Invariant variation problems. *Transport Theory and Statistical Physics*, 1(3):186–207, jan 1971.

- [96] I. Nutini. Study of charged particles interaction processes on ar in the 0.2 - 2.0 GeV energy range through combined information from ionization free charge and scintillation light. Technical report, jan 2015.
- [97] D. R. Nygren. The time projection chamber: A new 4π detector for charged particles. Technical report, 1974.
- [98] L. Onsager. Initial recombination of ions. *Phys. Rev.*, 54:554–557, Oct 1938.
- [99] S. Pascoli, S.T. Petcov, and A. Riotto. Leptogenesis and low energy cp-violation in neutrino physics. *Nuclear Physics B*, 774(1):1 – 52, 2007.
- [100] C. Patrignani et al. Review of Particle Physics. *Chin. Phys.*, C40(10):100001, 2016.
- [101] B. Pontecorvo. Neutrino Experiments and the Problem of Conservation of Leptonic Charge. *Sov. Phys. JETP*, 26:984–988, 1968. [Zh. Eksp. Teor. Fiz.53,1717(1967)].
- [102] T. Yang R. Acciarri. Investigation of the non-uniformity observed in the wire response to charge in lariat run 1. Technical report, February 2017.
- [103] T. Yang R. Acciarri, M. Stancari. Determination of the electron lifetime in lariat. Technical report, March 2016.
- [104] Martti Raidal. Relation between the neutrino and quark mixing angles and grand unification. *Phys. Rev. Lett.*, 93:161801, Oct 2004.
- [105] Steve Ritz et al. Building for Discovery: Strategic Plan for U.S. Particle Physics in the Global Context. 2014.
- [106] C. Rubbia. The Liquid Argon Time Projection Chamber: A New Concept for Neutrino Detectors. 1977.

- 1322 [107] L.M. Saunders. Electromagnetic production of pions from nuclei. *Nucl. Phys.*,
1323 *B7: 293-310(1968)*.
- 1324 [108] Qaisar Shafi and Zurab Tavartkiladze. Neutrino democracy, fermion mass hier-
1325 archies, and proton decay from 5d su(5). *Phys. Rev. D*, 67:075007, Apr 2003.
- 1326 [109] Sigma-Aldrich, P.O. Box 14508, St. Louis, MO 63178 USA.
- 1327 [110] R. K. Teague and C. J. Pings. Refractive index and the lorentz-lorenz function
1328 for gaseous and liquid argon, including a study of the coexistence curve near the
1329 critical state. *The Journal of Chemical Physics*, 48(11):4973–4984, jun 1968.
- 1330 [111] J. Thomas and D. A. Imel. Recombination of electron-ion pairs in liquid argon
1331 and liquid xenon. *Phys. Rev. A*, 36:614–616, Jul 1987.
- 1332 [112] D.R.O. Morrison N. Rivoire V. Flaminio, W.G. Moorhead. Compilation of
1333 Cross Sections I: π^+ and π^- Induced Reactions. *CERN-HERA*, pages 83–01,
1334 1983.
- 1335 [113] D.R.O. Morrison N. Rivoire V. Flaminio, W.G. Moorhead. Compilation of
1336 Cross Sections II: K^+ and K^- Induced Reactions. *CERN-HERA*, pages 83–02,
1337 1983.
- 1338 [114] Hermann Weyl. Gravitation and the electron. *Proceedings of the National*
1339 *Academy of Sciences of the United States of America*, 15(4):323–334, 1929.
- 1340 [115] Colin et al Wilkin. A comparison of pi+ and pi- total cross-sections of light
1341 nuclei near the 3-3 resonance. *Nucl. Phys.*, B62:61–85, 1973.
- 1342 [116] D. H. Wright and M. H. Kelsey. The Geant4 Bertini Cascade. *Nucl. Instrum.*
1343 *Meth.*, A804:175–188, 2015.

- 1344 [117] C. S. Wu, E. Ambler, R. W. Hayward, D. D. Hoppes, and R. P. Hudson.
1345 Experimental test of parity conservation in beta decay. *Phys. Rev.*, 105:1413–
1346 1415, Feb 1957.
- 1347 [118] N Yahlali, L M P Fernandes, K Gonzlez, A N C Garcia, and A Soriano. Imaging
1348 with sipms in noble-gas detectors. *Journal of Instrumentation*, 8(01):C01003,
1349 2013.
- 1350 [119] T. Yanagida. Horizontal symmetry and masses of neutrinos. *Progress of Theo-*
1351 *retical Physics*, 64(3):1103–1105, sep 1980.